Nucleotide excision repair: from molecular mechanisms to patient phenotypes

Apelt, K.

Chapter 2

XPC–PARP complexes engage the chromatin remodeler ALC1 to catalyze robust global genome DNA damage repair

Charlotte Blessing*, Katja Apelt*, Román González-Prieto, Adi Yifrach, Avital Parnas, Rashmi G. Shah, Melanie van der Woude, Angela Kragten, Hyun-Suk Kim, Alfred C.O. Vertegaal, Orlando D. Schärer, Hannes Lans, Girish M. Shah, Sheera Adar, Andreas G. Ladurner and Martijn S. Luijsterburg

- under revision at Nature Communications -

**Shared first author*

Abstract

Cells employ global genome DNA damage repair (GGR) to eliminate a broad spectrum of DNA lesions, including those induced by UV light. The lesion-recognition factor XPC initiates repair of helix-destabilizing DNA lesions, but binds poorly to lesions such as CPDs that do not destabilize DNA. How difficult-to-repair lesions are detected in chromatin is unknown. Here, we identify the poly-(ADP-ribose) polymerases PARP1 and PARP2 as constitutive interactors of XPC. The biochemical interaction between these proteins results in the PARylation of XPC at UV lesions and an XPC-dependent stimulation of the poly-(ADP-ribose) response. This enables the recruitment of the poly-(ADP-ribose)-regulated chromatin remodeler ALC1. Notably, we found that both PARP2 and ALC1 are required for the efficient clearing of CPD lesions. Our experiments reveal a molecular bookmarking system that primes chromatin containing difficult-to-repair DNA lesions for efficient repair, providing key molecular insights into the mechanism of how GGR is catalyzed at the level of chromatin plasticity.

Introductions

The integrity of the human genome is constantly threatened by endogenous and exogenous sources, which cause up to 10^5 DNA lesions per cell per day (Hoeijmakers, 2009). Cells thus critically depend on the accuracy of dedicated DNA repair mechanisms to recognize and remove genomic DNA lesions and maintain genome integrity (Ciccia and Elledge, 2010).

One principal source of DNA damage is UV light, which results in the crosslinking of neighboring bases on the same DNA strand, forming so-called 6-4 photoproducts (6-4PPs) and cyclobutane pyrimidine dimers (CPDs). Nucleotide excision repair (NER) can repair these bulky lesions (Scharer, 2013). The initiation of this repair pathway depends on the position of the lesion in the genome. While RNA polymerase II stalling at lesions in transcribed strands initiates transcription-coupled repair (TCR or TC-NER) (van der Weegen et al., 2020), lesions in transcriptionally inactive genome regions are recognized by specialized damage sensors that initiate global genome repair (GGR or GG-NER) (Sugasawa et al., 1998). Recognition through both sub-pathways ultimately leads to a common pathway of verification, excision and re-synthesis of the damaged DNA. In principle, all core NER factors have been identified and the fundamental DNA repair process can be reconstituted *in vitro* (Aboussekhra et al., 1995; Mu et al., 1995). However, the cellular repair mechanism is not well understood in the chromatin context, as knowledge about chromatin factors that allow and promote the efficient action of the core repair factors is limited.

In mammalian cells, GGR is initiated by XPC, which forms a complex with RAD23B and CEN2 (Araki et al., 2001; Masutani et al., 1994; Sugasawa et al., 1998; Volker et al., 2001). Rather than binding to lesions directly, XPC binds the accessible, non-damaged DNA that is opposite the DNA injury. This allows the recognition of a broad spectrum of lesions that are structurally unrelated (Maillard et al., 2007; Min and Pavletich, 2007). XPC binding results in the slight opening of the DNA surrounding a lesion (~6 nucleotides) (Tapias et al., 2004), which facilitates the binding of subsequent factors. The recruitment of these downstream NER proteins, including TFIIH, RPA, XPA, XPG and ERCC1-XPF, to sites of UV-induced DNA lesions is abolished in XPC-deficient cells. This demonstrates that the GGR repair pathway is strictly dependent on XPC (Volker et al., 2001).

Although XPC has a high affinity for 6-4PPs, its binding to CPDs is rather inefficient due to minimal thermodynamic helix destabilization. The recognition and repair of CPDs therefore requires the additional action of

the damaged-DNA binding protein 2 (DDB2) (Tang et al., 2000), which does not seem to influence *in vitro* reconstituted NER (Aboussekhra et al., 1995). DDB2 further utilizes slide-assisted site exposure to detect even inaccessible lesions occluded in nucleosomes (Matsumoto et al., 2019), and creates a local chromatin environment around lesions that facilitates the assembly of repair complexes (Adam et al., 2016; Luijsterburg et al., 2007; Luijsterburg et al., 2012; Wang et al., 2006). DDB2 is thus often considered as factor that prepares chromatin for GGR, but its dissociation from DNA lesions is subsequently required for repair to proceed further (Ribeiro-Silva et al., 2020). Whether this is an exclusive feature of DDB2 or whether and how XPC also contributes to local chromatin changes is unknown.

In addition to XPC and DDB2, PARP1 is also able to associate with UV-induced DNA lesions (Purohit et al., 2016; Robu et al., 2017; Vodenicharov et al., 2005). *In vitro* approaches showed that PARP1 and DDB2 can simultaneously bind to a UV-induced CPD (Purohit et al., 2016). In agreement, *in situ* fractionation showed that endogenous PARP1 is recruited to sites of local UV damage (Purohit et al., 2016; Robu et al., 2017; Robu et al., 2020). However, the precise interplay between these three lesion-recognition proteins during GGR is poorly understood. Initially, DDB2 was found to associate with and potentially stimulate the catalytic activity of PARP1, resulting in the poly-(ADP-ribos) ylation (PARylation) of DDB2. This was suggested to counteract DDB2 auto-ubiquitylation and its subsequent degradation (Pines et al., 2012). Consistently, inhibition of PARP activity was found to accelerate DDB2 degradation (Pines et al., 2012) and to reduce XPC recruitment to UV lesions under conditions of low damage load (Luijsterburg et al., 2012; Robu et al., 2013). PARP1 was shown to stimulate XPC recruitment to DNA damage sites in a DDB2-independent manner and to regulate XPC release (Robu et al., 2017). Thus, it appears that both DDB2 and PARP1 may stimulate XPC recruitment to initiate GGR. However, the relevance of the poly-(ADP-ribose) response for GGR and to what extent this is regulated by XPC remains to be established.

In addition to PARP1, the nuclear and DNA damage-dependent PARP2 enzyme seems to have independent functions in the DNA damage response, which are not well understood. In general, PARP1 is thought to provide about 90% of the PAR signal at DNA lesions, while PARP2 contributes a minor part (Ame et al., 1999; Shieh et al., 1998). Instead, PARP2 is suggested to increase the branching of PAR chains (Chen et al., 2018). The double knockout of both PARP1 and PARP2 is embryonic lethal in mice (Menissier de Murcia et al., 2003) and highly sensitizes cells to DNA-damaging agents, such as the alkylating agent

methyl methanesulfonate (MMS) (Ronson et al., 2018). This suggests that both proteins cooperatively act in the DNA damage response. However, whether PARP2 contributes to the poly-(ADP-ribose) response and has roles in GGR remains to be established.

Here, we sought to establish the role for PARylation, PARP2 and active chromatin remodeling in UV-induced GGR. Using proteomics, live-cell imaging and UV-induced DNA damage, our data revealed a new XPC-PARP axis that links ALC1-mediated chromatin remodeling to GGR. We identify the poly-(ADP-ribose) polymerases PARP1 and PARP2 as constitutive interactors of the damage-recognition protein XPC. The close interaction between these proteins results in the PARylation of XPC at UV lesions and an XPC-dependent stimulation of the poly-(ADP-ribose) response, which facilitate the recruitment of the poly-(ADP-ribose)-dependent chromatin remodeler ALC1. Both ALC1 and in particular PARP2 are required for the efficient clearing of difficult-to-repair CPD lesions. We thus identify a new XPC-dependent mechanism that impacts the chromatin environment and promotes chromatin remodeling at UV lesions.

Results

XPC interacts with PARP1 and PARP2

To identify potential new factors involved in GGR, we sought to identify the interactome of the damage-recognition factor XPC by mass spectrometry. We generated a knockout (KO) of XPC in U2OS(FRT) cells containing an FRT Flp-In integration site. Having confirmed the successful knockout of XPC by sequencing and western blot analysis (Figure S1a), we exploited the site-specific transgene integration of the Flp-In system to re-express XPC-GFP in these cells under a doxycycline-inducible promoter. To demonstrate the functionality of our newly generated cell system, we measured the ability to repair UV lesions in unscheduled DNA synthesis (UDS) assays. While the XPC-KO showed a severe repair defect, the re-expression XPC-GFP restored the capacity of the cells to repair UV-induced DNA damage (Figures S1b, S1c). Label-free proteomics after pull-down of XPC-GFP revealed several known XPC-binding proteins, including RAD23A/B and CEN2/3, as the top interactors (Figure 1a). After UV irradiation, XPC additionally became tightly bound to several GGR factors, such as the DDB2 complex (containing DDB1 and CUL4A/B), the TFIIH subunits GTF2H1-4 (p62, p44, p34, p52), XPB (p89/ERCC3)

Figure 1

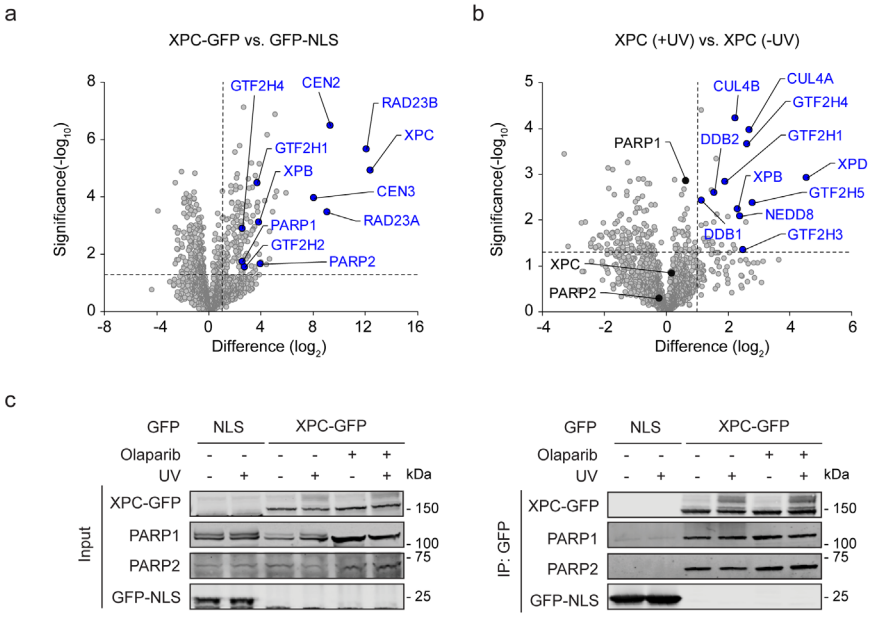

Figure 1: XPC interacts with PARP1 and PARP2 in a UV-independent manner. (a) Volcano plot displaying the interactome of XPC-GFP over GFP-NLS after GFP-pulldown from U2OS (FRT) XPC-KO cells and analysis by label-free proteomics. (b) Differential interactome of XPC-GFP comparing UVC-irradiated (20 J/m^2, 1h) vs. unirradiated U2OS (FRT) XPC-KO cells. (a, b) The dashed lines indicate a 2-fold enrichment on the x-axis ($\log_2$ of 1) and a significance of 0.05 ($-\log_{10}$ P value of 1.3) on the y-axis. (c) Co-Immunoprecipitation (Co-IP) of GFP-NLS and XPC-GFP in the presence and absence of UV-C (20 J/m^2, 1 h) and the PARP inhibitor olaparib (10 μM).

and XPD (p80/ERCC2) (Figure 1b). This confirms that our label-free proteomics approach is suitable to detect interactions within an active GGR process.

Interestingly, our analysis further identified the poly-(ADP-ribose) polymerases PARP1 and PARP2 as strong XPC-associated proteins (Figure 1a). In contrast to the main GGR factors, the interaction between XPC and PARP1/2 was not significantly affected by UV irradiation (Figure 1b). Immunoprecipitation experiments confirmed that the XPC-PARP1/2 interaction was constitutive and independent of PARylation, as treatment with the PARP inhibitor olaparib did not affect the interactions (Figure 1c). Our findings indicate that XPC forms a constitutive interaction with both PARP1 and PARP2, which is neither affected by DNA damage, nor by PARylation.

XPC and ALC1 interact more strongly with PARP2 than PARP1

To obtain first insights into the role of PARP1 and PARP2 in GGR and the relevance of their interaction with XPC, we conducted an orthogonal experiment to identify the interactome of the two PARP enzymes. We stably expressed PARP1-GFP or GFP-PARP2 in U2OS(FRT) cells (Figure S2a) and performed label-free proteomics after GFP-pulldown of the tagged proteins. PARP1 most abundantly interacted with XRCC1-LIG3 and POLB, and further showed robust interactions with PARP2, histones, as well as the known poly-(ADP-ribose)-binding proteins ALC1 and macroH2A (Figure 2a). In contrast, XPC was not significantly enriched in the PARP1 interactome (Figures 2a, 2b), which is likely caused by the high abundance of PARP1 and a potentially low stoichiometric interaction with XPC. It should be noted that earlier studies did report an interaction between immunoprecipitated endogenous PARP1 and XPC (Robu et al., 2017).

Interestingly, the interactome of PARP2 revealed the poly-(ADP-ribose)-dependent chromatin remodeler ALC1 as its most abundant interactor. PARP2 further interacted with XRCC1-LIG3, PARP1, histones and macroH2A (Figure 2c). PARP2 also clearly interacted with XPC in a manner that was not affected by UV irradiation (Figures 2c, 2d). Intensity-based absolute quantification (iBAQ) of protein amounts indicated that ~15% of the isolated PARP2 molecules associated with ALC1, while only 0.07% of PARP1 molecules interacted with the remodeler (Figure 2e). Additionally, the fraction of PARP2 molecules that associated with XPC was ten-fold higher than for PARP1. The stoichiometry among PARP enzymes was very low with 1.76% of the PARP2 molecules interacting with PARP1, ruling out indirect interactions through PARP heterodimerization. Immunoprecipitation experiments confirmed that PARP2 robustly interacted with both ALC1 and XPC, while these interactions were not or only weakly detected after pull-down of PARP1 (Figure 2f). This demonstrates that XPC and ALC1 both preferentially associate with PARP2 over PARP1 under our experimental conditions.

PARP1/2 recruitment to UV lesions is independent of XPC

The DNA damage-recognition proteins XPC and DDB2 can both bind to UV-induced lesions. DDB2 thereby stimulates XPC recruitment at difficult-to-detect lesions, such as CPDs (Luijsterburg et al., 2012; Moser et al., 2005; Tang et al., 2000), and facilitates lesion recognition by XPC in a chromatin context. PARP1 was also reported to bind to UV-induced DNA lesions together with XPC (Purohit et al., 2016; Robu et al., 2017). Considering the interaction between XPC and PARP1/2, we asked whether the PARP enzymes are recruited to UV lesions and if this is stimulated by XPC. To

Figure 2

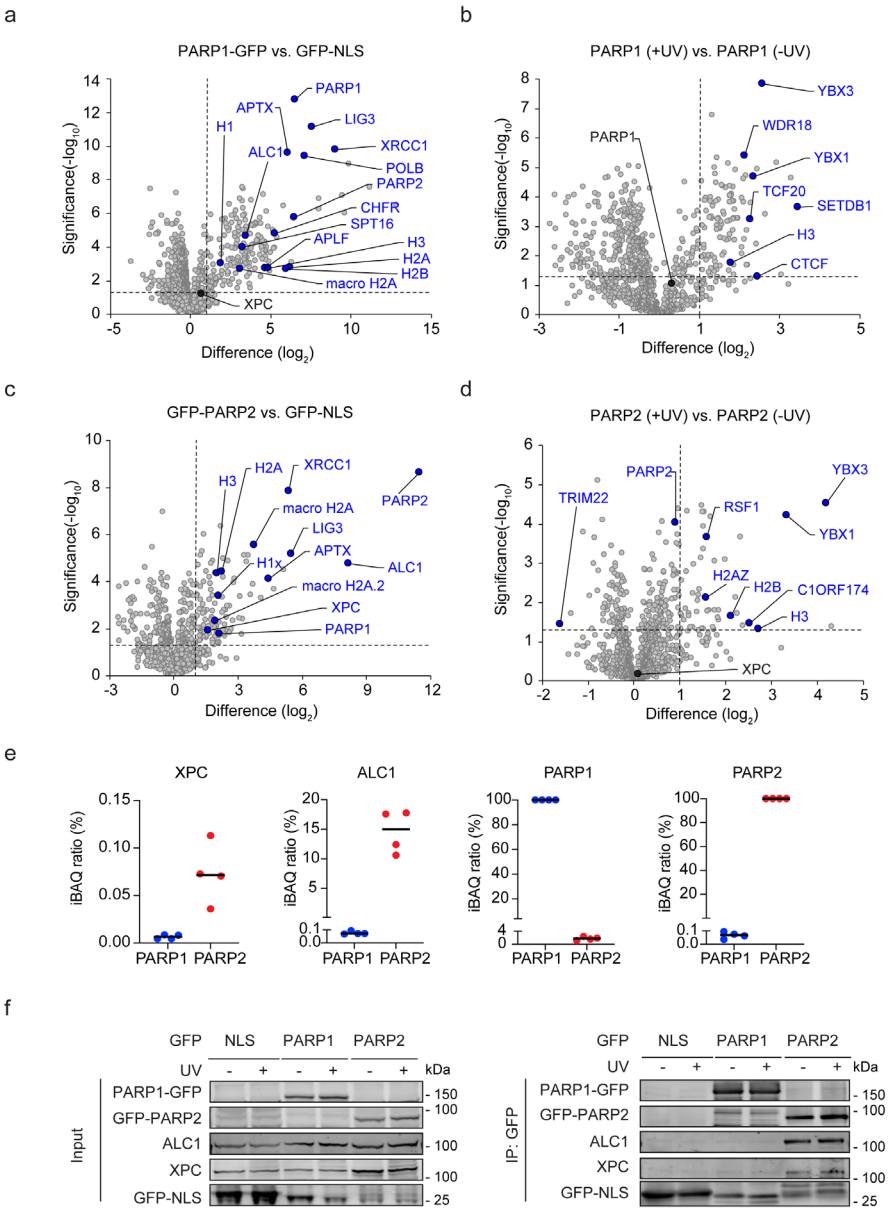

Figure 2: XPC and ALC1 interact more strongly with PARP2 than PARP1. (a, c) Volcano plots displaying the interactomes of (a) PARP1-GFP and (c) GFP-PARP2 after GFP-pulldown from U2OS (FRT) WT cells and analysis by label-free proteomics. (b, d) Differential interactomes of (b) PARP1-GFP and (d) GFP-PARP2 from UVC-irradiated (20 J/m^2, 1h) vs. unirradiated U2OS (FRT) WT cells. (a-d) The dashed lines indicate a 2-fold

enrichment on the x-axis (log_2 of 1) and a significance of 0.05 ($-log_{10}$ P value of 1.3) on the y-axis. (e) Enrichment of XPC, ALC1, PARP1 and PARP2 in the co-IPs of PARP1 (a) and PARP2 (b), calculated by intensity-based quantification (IBAQ). Each data point represents a biological replicate. (f) Co-IP of GFP-NLS, PARP1-GFP and GFP-PARP2 in the presence and absence of UVC (20 J/m^2, 1h).

this end, we employed a UV-C (266 nm) laser live-cell imaging set-up, in which all optics have been replaced by quartz glass. Local irradiation with UV-C led to the rapid recruitment of PARP1-GFP within seconds, after which steady-state bound levels decreased in the first several minutes (Figures 3a, 3b). GFP-PARP2 was also recruited to UV-C laser damage. Steady-state bound levels remained high for ~10 min without an apparent decrease (Figures 3c, 3d). The enrichment of PARP1-GFP shortly after UV-C micro-irradiation was more pronounced (1.4-fold) compared to the more modest recruitment of PARP2-GFP (1.2-fold). Interestingly, the recruitment kinetics of PARP1 and PARP2 were identical in XPC-KO cells (Figures 3c, 3d). This indicates that PARP enzymes accumulate independently of XPC at sites of UV-induced DNA damage, which is in line with earlier findings showing that PARP1 recruitment is similar between WT and XP-C cells at 10 min after UV irradiation (Robu et al., 2017). Deletion of either PARP1 or PARP2 had a minor impact on the recruitment of XPC to UV lesions, as measured by immunofluorescence after local UV irradiation through micropore filters (Figures 3e, 3f). The impact of PARP enzymes was milder than KO of DDB2, which led to considerably reduced XPC recruitment, as reported previously (Luijsterburg et al., 2012; Moser et al., 2005; Tang et al., 2000). Our data thus suggest that XPC and PARP enzymes are recruited to DNA lesions largely independently, although PARP enzymes may stimulate XPC recruitment under certain conditions, such as low doses of DNA damage (Luijsterburg et al., 2012; Robu et al., 2017).

XPC is a UV-induced substrate of PARylation

The PARP response involves the rapid and robust DNA damage-induced PARylation mainly of PARP1 itself, but also of other chromatin substrates (Ray Chaudhuri and Nussenzweig, 2017). To better understand how the PARP response modulates GGR, we measured nuclear PAR levels by immunofluorescence in PARP1-KO and PARP2-KO cells (Figure S2b). PARylation strongly increased after UV irradiation in WT cells and PARP2-KO cells, but not in PARP1-KO cells (Figures 4a, 4b and S2c). This demonstrates that the PAR response at UV lesions is largely dependent on PARP1, as demonstrated for other DNA damaging agents (El-Khamisy et al., 2003; Luijsterburg et al., 2016).

Based on the close interaction of XPC and PARP1/2, we next

Figure 3

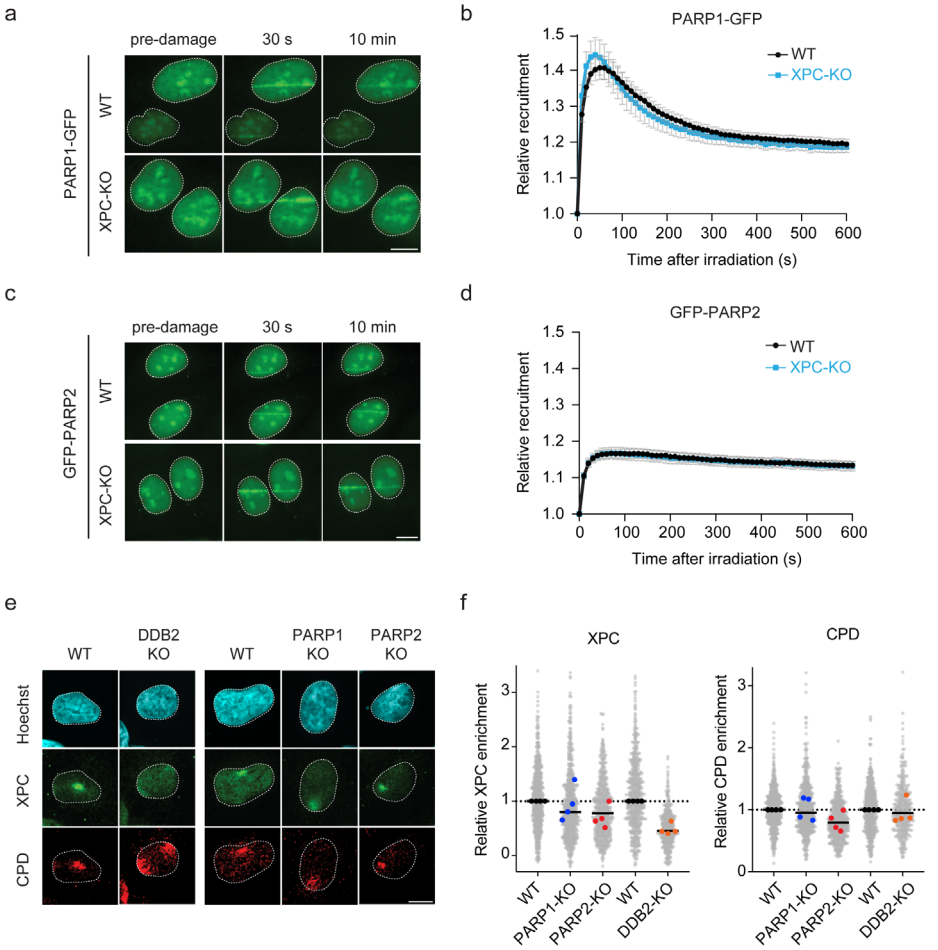

Figure 3: PARP1/2 recruitment to UV lesions is independent of XPC. (a, c) Representative images of (a) PARP1-GFP and (c) GFP-PARP2 association with sites of local UVC laser irradiation in U2OS (FRT) WT and XPC-KO cells at 30 sec and 10 min post-irradiation. (b, d) Kinetics of the recruitment of (b) PARP1-GFP and (d) GFP-PARP2 to and dissociation from UVC lesions measured over 10 min in U2OS (FRT) WT and XPC-KO cells; 70-91 nuclei were analyzed in three independent biological replicates. The data are shown as mean + SEM normalized to pre-damage GFP intensity at micro-irradiation sites. (e) Representative images and (f) quantification of XPC co-localization with local UV-C irradiation sites (100 J/m^2) marked by CPD, measured 10 min post-irradiation. 58-230 cells were analyzed per condition. All cells are depicted as individual data points (grey). The medians of four biological replicates are depicted as colored points, while the bar represents the median of all data points.

Figure 4

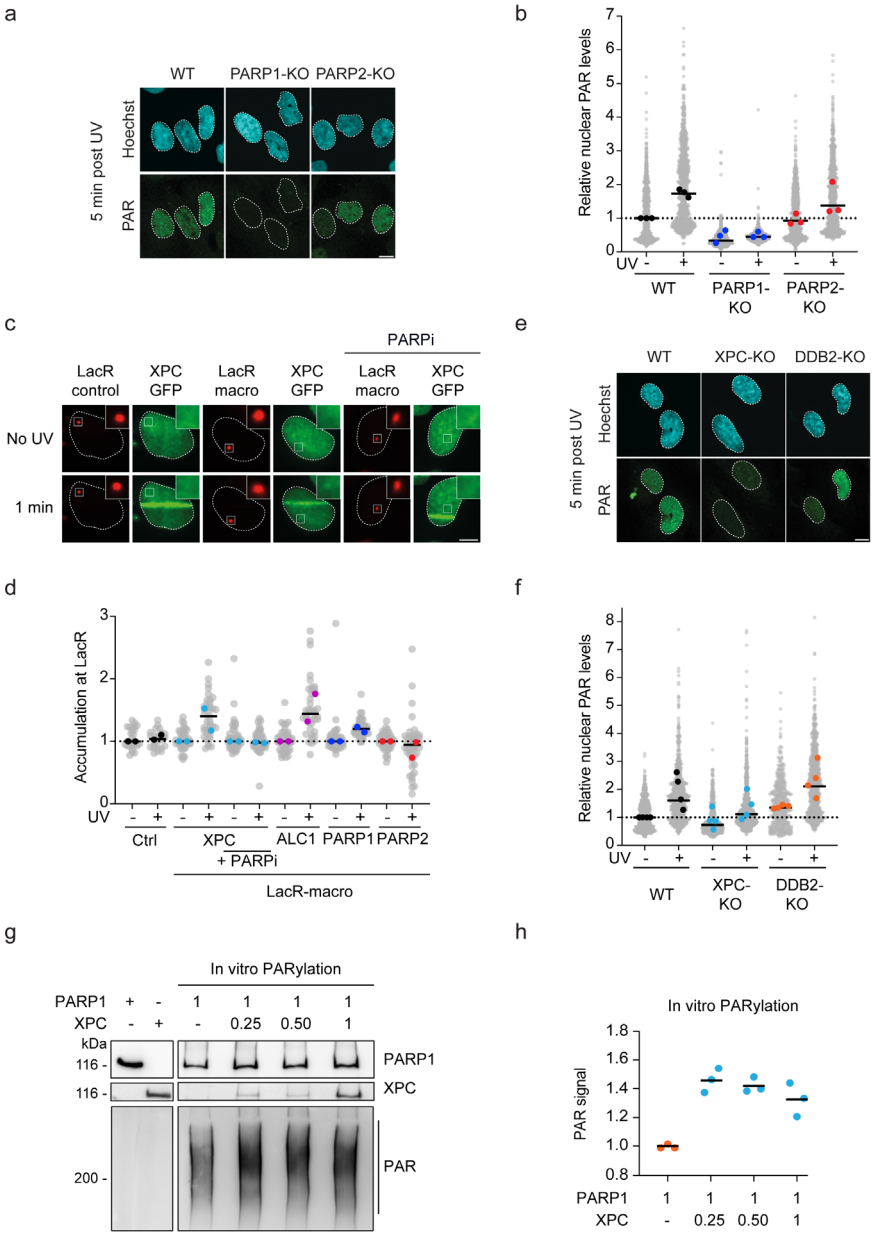

Figure 4: XPC stimulates the poly-(ADP-ribose) response at UV lesions. (a) Representative images and (b) quantification of poly-(ADP-ribose) (PAR) levels 5 minutes after UVC irradiation (20 J/m^2) by immunofluorescence in U2OS WT, PARP1-KO and PARP2-KO cells. >75 cells were analyzed per condition from three independent experiments. Additional representative images are found in Figure S2c. (c) Representative images and (d) quantification of GFP-tagged XPC, ALC1, PARP1 or PARP2 recruitment

to the LacO array upon tethering to the indicated mCherry-LacR-macrodomain. Pictures were taken before and 1 min after UV-C micro-irradiation. 24-45 nuclei were analyzed in two independent biological replicates. Additional representative images are found in Figure S2e. (e) Representative images and (f) quantification of poly-(ADP-ribose) (PAR) levels 5 minutes after UVC irradiation (20 J/m^2) by immunofluorescence in U2OS (FRT) WT, XPC-KO and DDB2-KO cells. >65 cells were analyzed per condition from four independent experiments.

asked whether XPC could be a substrate for PARylation upon UV damage. We therefore performed an adapted LacO-based colocalization assay, in which we fused the PAR-binding macrodomain of macroH2A1.1 to LacR and tethered this PAR-binding module to a LacO array in U2OS 263 cells (Janicki et al., 2004; Smith et al., 2018). We then induced the PARylation response by local irradiation with a 266 nm UV-C laser. Micro-irradiation triggered the recruitment of GFP-tagged versions of XPC, ALC1, PARP1 and PARP2 to sites of UV-C-induced laser damage (Figures 4c, 4d and S2e). Within one minute following irradiation, we also detected the capture of XPC, ALC1 and PARP1 at the LacO array bound by the LacR-fused macrodomain PAR-binding module. This suggests that XPC, ALC1 and PARP1 become PARylated at laser micro-irradiation sites and dissociate from these sites in a modified, PARylated state, which in turn allows their interaction with the immobilized macrodomain at the LacO array. Treatment with the PARP inhibitor olaparib prevented the accumulation of XPC at the LacO site, demonstrating that its capture at the LacO array is fully dependent on PARylation (Figures 4c, 4d). Interestingly, PARP2 was recruited to UV sites, but could not be detected at the LacO site following micro-irradiation, suggesting that its UV-induced PARylation is not sufficiently high or that it is rapidly reversed, thereby preventing the capture of PARP2 by the immobilized PAR-binding module at the LacO array.

XPC stimulates the poly-(ADP-ribose) response at UV lesions

Having established that XPC is PARylated at UV lesions, we sought to investigate whether XPC impacts the PAR response. Strikingly, XPC-KO cells showed an attenuated PAR response after UV, while DDB2-KO cells established PAR levels similar to wild-type U2OS cells (Figures 4e, 4f and S2d).

To understand whether XPC may directly stimulate the activity of PARP enzymes through their interaction, we performed *in vitro* PARylation assays using recombinant PARP1 in the presence of UV-irradiated DNA and increasing amounts of recombinant XPC-RAD23B complex (Figures 4g, 4h). In this minimal *in vitro* system without additional components, we observed that XPC directly stimulated the catalytic activity of PARP1 by ~1.5 fold, which was already observed at a 4:1 ratio of PARP1 over XPC-

Figure 5

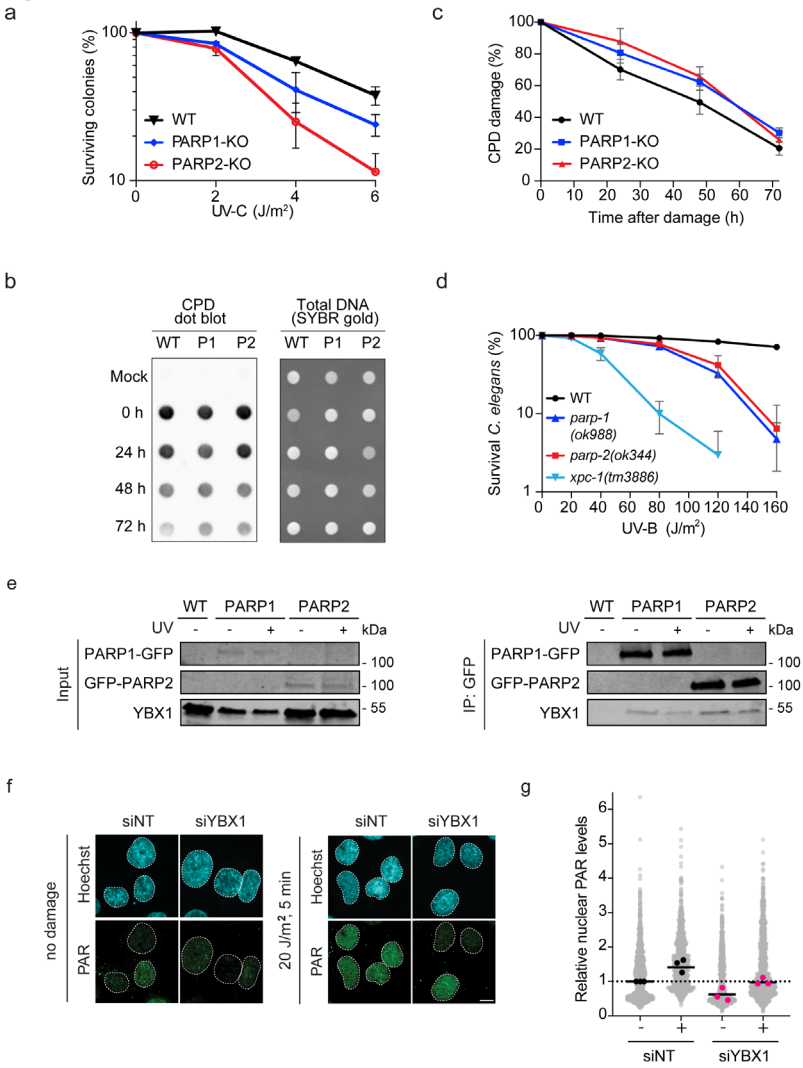

Figure 5: PARP1 and PARP2 impact the repair of CPD lesions. (a) Clonogenic survival assays of U2OS WT, PARP1-KO and PARP2-KO cells upon UV-C irradiation. The data is depicted as mean + SEM. from 3-4 independent experiments. (b) Representative dot blots and (c) quantification of CPD levels in U2OS WT, PARP1-KO and PARP2-KO cells at different time points after UV-C damage (20 J/m^2). The data is depicted as mean + SEM of four independent experiments. (d) Germ cell and embryo UV survival assays of PARP1-deficient parp-1(ok988) and PARP2-deficient parp-2(ok344) C. elegans. The data is depicted as mean + SEM from three independent experiments (e) Co-IP of PARP1-GFP and GFP-PARP2 in the presence and absence of UVC (20 J/m^2, 1h). (f) Representative images of and (g) quantification of PAR levels 5 min after UVC irradiation (20 J/m^2) by immunofluorescence in U2OS (FRT) WT cells targeted with either non-targeting or YBX1 siRNAs. >160 cells were analyzed per condition from three independent experiments. All

cells are depicted as individual data points (grey). The median of each biological replicate is depicted as a colored point, while the bar represents the median of all data points.

RAD23B complex and did not increase when more XPC was added to the reaction (Figures 4g, 4h). These findings show that XPC stimulates the initial and rapid PAR response at UV lesions, both by being a substrate for PARylation itself and by enhancing the protein activity of PARP1.

PARP1 and PARP2 stimulate CPD repair

To establish the relevance of PARP1 and PARP2 in UV damage repair, we first assayed PARP1-KO and PARP2-KO cells for UV sensitivity. Clonogenic survival assays showed that KO of either PARP1 or more strongly PARP2 conferred sensitivity to UV irradiation (Figure 5a). To validate these findings, we performed immunoblot assays in PARP1-KO and PARP2-KO cells. To this end, genomic DNA was isolated from cells at varying timepoints after UV-C irradiation to determine the amount of remaining UV-induced photoproduct. This immunoblot approach revealed that both PARP1-KO and PARP2-KO cells displayed delayed CPD repair (Figures 5b, c). In line with our clonogenic survival assays, PARP2-KO cells showed a stronger CPD repair defect than PARP1-KO cells. These data suggest that both PARP1 and PARP2 play an important role in the efficient repair of difficult-to-repair CPDs.

To extend the biological relevance of these findings, we asked whether the role of PARP1 and PARP2 in protecting against UV irradiation is evolutionary conserved in an animal model. To this end, we obtained PARP1-deficient (ok988) and PARP2-deficient (ok344) C. elegans and performed germ cell and embryo survival assays after UV irradiation, which specifically monitor GGR (Sabatella et al., 2021). Interestingly, deletion of either PARP1 or PARP2 strongly sensitized nematodes to UV-B light compared to WT animals (Figure 5d). This indicates a strong evolutionary conservation of the involvement of both PARP enzymes in GGR.

YBX1 regulates the UV-induced PAR response

To gain more insight into the UV-induced PAR response and to identify potential PARP1/2 co-factors, we performed label-free proteomics after pulldown of PARP1 and PARP2 following UV irradiation. After UV irradiation, both PARP1 and PARP2 became strongly bound to the RNA-binding protein YBX1 (Figures 2b, 2d), which has been suggested to enhance the PARylation activity of PARP1 *in vitro* (Naumenko et al., 2020). Immunoprecipitation of PARP1 or PARP2 confirmed an interaction with YBX1 (Figure 5e). Knockdown of YBX1 by siRNA led to reduced nuclear PAR levels and a reduced PAR response after UV irradiation (Figures 5f,

Figure 6

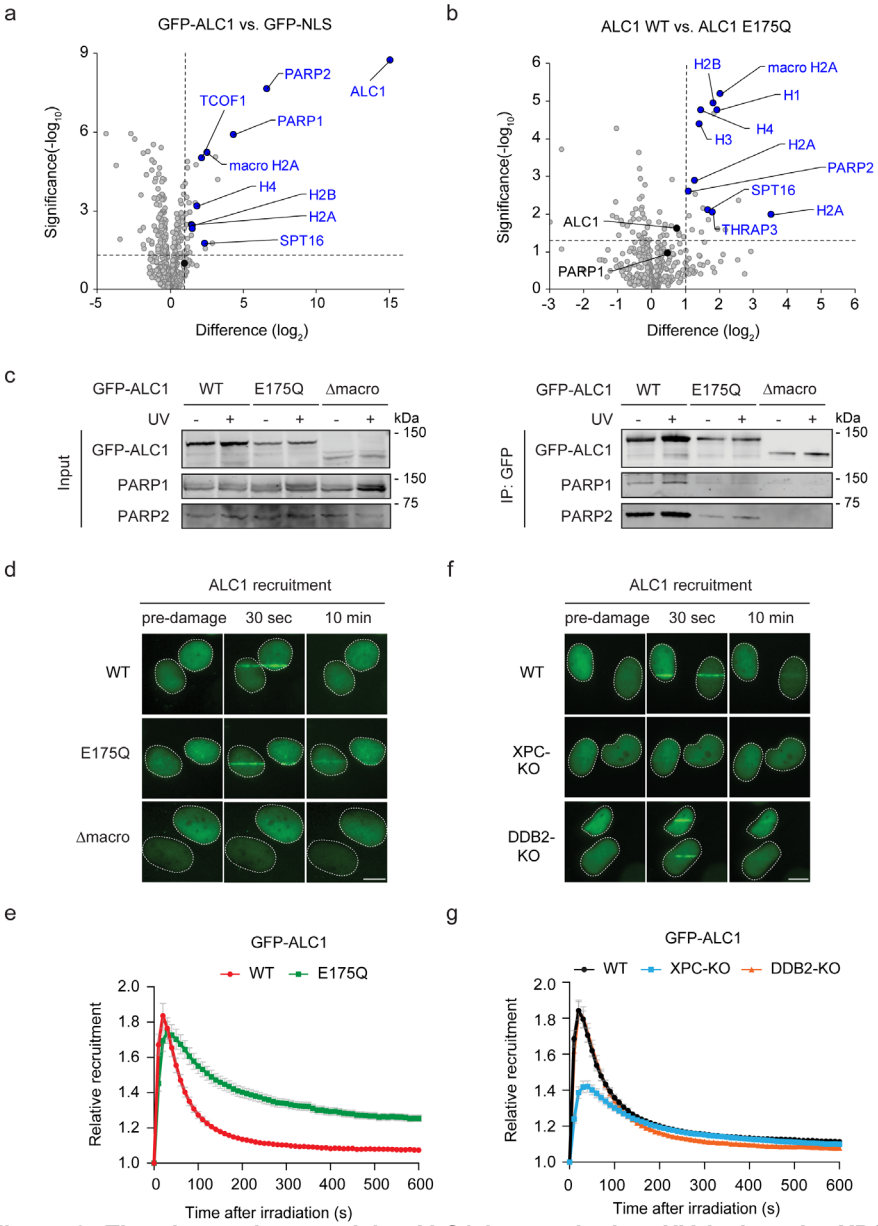

Figure 6: The chromatin remodeler ALC1 is recruited to UV lesions by XPC. (a) Volcano plot displaying the interactomes of GFP-ALC1 over GFP-NS after GFP-pulldown from U2OS (FRT) ALC1-KO cells and analysis by label-free proteomics. (b) Differential interactome of GFP-ALC1 WT vs. the catalytic-deficient GFP-ALC1 E175Q mutant. (a, b) The dashed lines indicate a 2-fold enrichment on the x-axis ($\log_2$ of 1) and a significance of 0.05 ($-\log_{10}$ P value of 1.3) on the y-axis. (c) Co-IP of GFP-ALC1 WT, GFP-ALC1 E175Q and a PAR-binding deficient GFP-ALC1 Δmacrodomain in the presence and

absence of UV-C (20 J/m^2, 1h). (d) Representative images and (e) recruitment kinetics of GFP-ALC1 WT, GFP-ALC1 E175Q, GFP-ALC1 ∆macrodomain at sites of local UVC laser irradiation in U2OS (FRT) ALC1-KO cells. 77-82 cells were analyzed in three independent experiments. (f) Representative images and (g) recruitment kinetics of GFP-ALC1 at sites of local UV-C laser irradiation in U2OS (FRT) WT, XPC-KO and DDB2-KO cells. 107-135 cells were analyzed in 4-6 independent experiments. The data are shown as mean + SEM normalized to pre-damage GFP intensity at micro-irradiation sites.

g and S2f). These data suggest that YBX1 is a new component of the PAR response.

ALC1 is recruited to UV lesions by XPC

To better understand the links between XPC and PARP enzymes and the effects of the poly-(ADP-ribose)-response on GGR, we turned our attention to the poly-(ADP-ribose)-dependent chromatin remodeler ALC1. Our proteomics analyses revealed that XPC binds more robustly to PARP2 than PARP1, and that ALC1 is an abundant interactor of PARP2 (Figures 2c, S1a). To study ALC1 in more detail, we generated ALC1-KO cells in U2OS(FRT) and stably re-expressed GFP-tagged versions of ALC1 (WT, ATPase-dead; E175Q, and PAR-binding deficient; Δmacrodomain; Figure S3a). Label-free proteomics after GFP-ALC1 pulldown confirmed a strong interaction of wild-type ALC1 with PARP2, PARP1, the FACT subunit SPT16 and core histones (Figure 6a). In contrast, the ATPase-dead version of ALC1 interacted less with PARP2, and core histones, suggesting that the ATPase activity of ALC1 impacts the enzyme's association with PARP2 (Figure 6b). Consistently, immunoprecipitation experiments confirmed that ALC1 robustly bound PARP2 and to a lesser extent PARP1, and that these interactions were decreased with ALC1-E175Q (Figure 6c). Moreover, a ALC1-∆macrodomain mutant showed a completely disrupted interaction with PARP1/2.

Next, we tested the recruitment of ALC1 to UV-C DNA damage sites. Local UV-C laser irradiation experiments showed that GFP-ALC1 was rapidly recruited with kinetics that closely followed the recruitment kinetics of PARP1 (Figures 6d, 6e). The ATPase-dead version of ALC1 was also rapidly recruited. However, its steady-state bound levels persisted for extended periods of time, while the macrodomain deletion mutant failed to recruit (Figures 6d, 6e). Our data suggest that the chromatin remodeler ALC1 is tightly linked to the poly-(ADP-ribose) response at UV lesions. The PAR-dependent recruitment of ALC1 via its macrodomain leads to a robust interaction with chromatin, which is then followed by ATP hydrolysis and localized chromatin remodeling. In turn, ATP hydrolysis by ALC1 results in the displacement and dissociation of the ALC1 chromatin remodeler from UV-damaged chromatin.

Figure 7

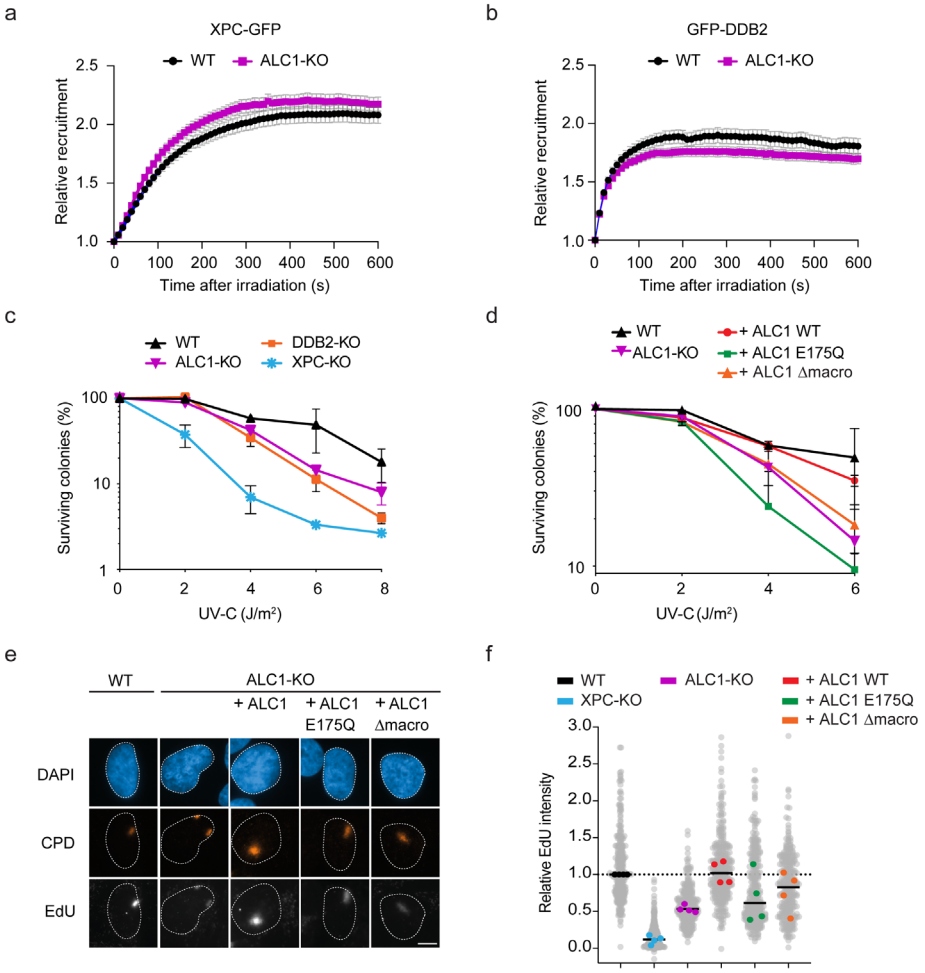

Figure 7: ALC1's ATPase activity stimulates XPC-dependent DNA repair. (a, b) Recruitment kinetics of (a) XPC-GFP and (b) GFP-DDB2 at sites of local UVC laser irradiation. 80-135 cells were analyzed in three independent experiments. The data are shown as mean + SEM normalized to pre-damage GFP intensity at micro-irradiation sites. (c, d) Clonogenic survival assays of (c) U2OS (FRT) WT, ALC1-KO, DDB2-KO and XPC-KO cells as well as (d) U2OS (FRT) WT, ALC1-KO, ALC1-KO + GFP-ALC1, ALC1-KO + GFP-ALC1 E175Q, ALC1-KO + GFP-ALC1 Δmacrodomain cells upon UVC irradiation. The data is depicted as mean + SEM from three independent experiments. (e) Representative images and (f) quantification of unscheduled DNA synthesis experiments in U2OS (FRT) WT, XPC-KO, ALC1-KO, ALC1-KO + GFP-ALC1, ALC1-KO + GFP-ALC1 E175Q, ALC1-KO + GFP-ALC1 Δmacrodomain cells upon UVC irradiation. >39 cells were analyzed in four independent experiments. All cells are depicted as individual data points (grey). The median of each biological replicate is depicted as a colored point, while the bar represents the median of all data points.

Figure 8

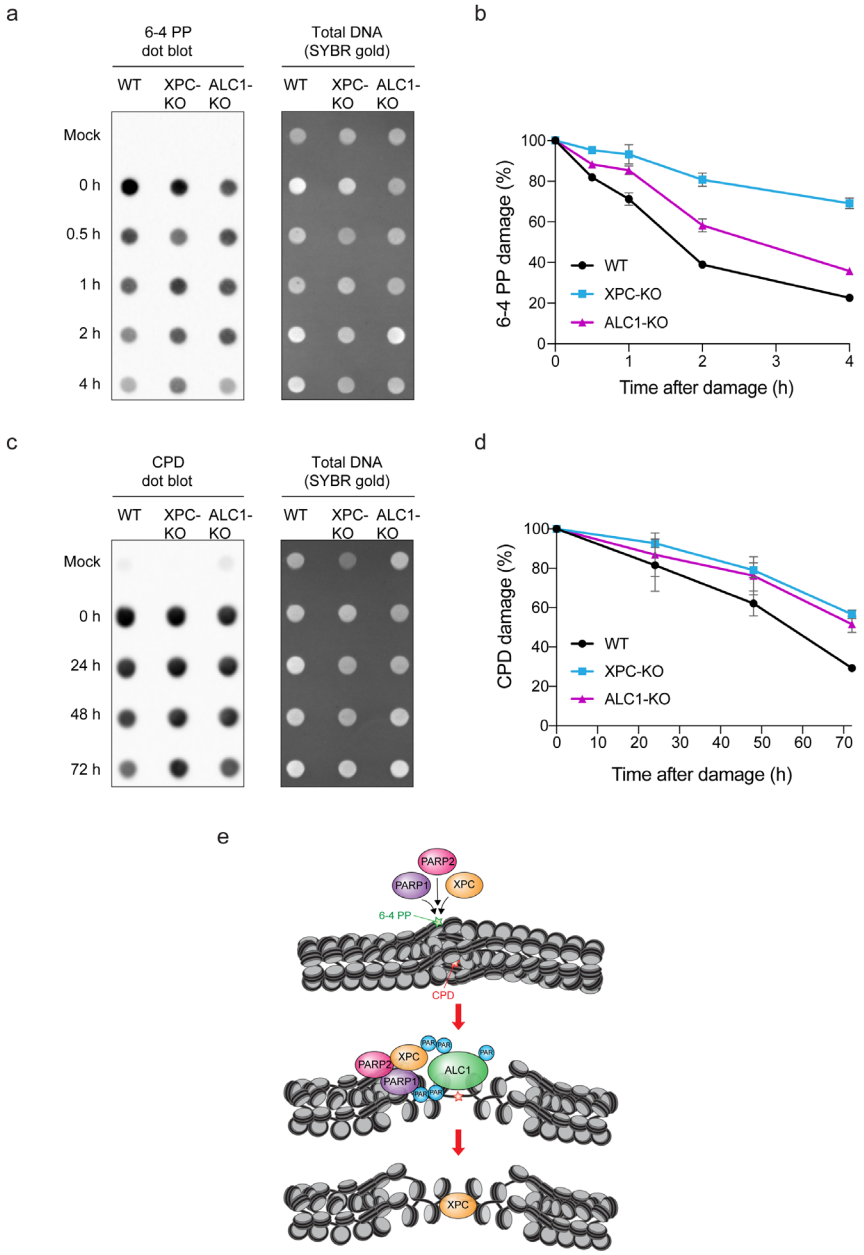

Figure 8: ALC1 is required for the repair of 6-4PP and CPD lesions. (a, c) Representative dot blots and (b, d) quantification of 6-4PP (a, c) and CPD (b, d) levels in U2OS (FRT) WT, ALC1-KO and XPC-KO cells at different time points after UV-C damage (20 and 10 J/m^2, respectively). The data is depicted as mean + SEM of 3-4 independent experiments. (e) Model of PARP1, PARP2 and ALC1 influence on XPC-dependent repair.

Further, the recruitment of ALC was fully impaired in PARP1-deficient cells, while its recruitment still occurred in PARP2-deficient cells, albeit with distinct kinetics (Figures S3b, S3c). This suggests that PARP2 may modulate ALC1 association dynamics. Strikingly, we also observed a strongly decreased recruitment of ALC1 in XPC-KO cells, while the recruitment of ALC1 in DDB2-KO cells was similar to WT (Figures 6f, 6g). Our data indicates that the GGR-initiator protein XPC stimulates the recruitment of chromatin remodeler ALC1 to sites of UV-induced DNA damage, suggesting that the XPC-mediated stimulation of the poly-(ADP-ribose) response promotes PAR-dependent downstream processes, such as ALC1-mediated chromatin remodeling.

ALC1's ATPase activity stimulates XPC-dependent DNA repair

Having found that XPC stimulates the recruitment of ALC1 to repair sites, we wanted to understand how ALC1-mediated chromatin remodeling affects UV damage repair. Importantly, loss of ALC1 function did not affect the recruitment of XPC or DDB2 following UV-C laser irradiation (Figures 7a, 7b, S4a, S4b). This suggested that XPC and DDB2 binding could precede ALC1 recruitment and that ALC1 does not affect the lesion-recognition step of GGR. However, clonogenic UV survival experiments revealed that the knockout of ALC1 rendered cells sensitive to UV irradiation to a similar extent as DDB2-KO cells (Figure 7c). Importantly, re-expression of ALC1-WT, but not the ATPase-dead or PAR binding-deficient ALC1 mutants, rescued both the UV-sensitive phenotype and the unscheduled DNA synthesis at UV sites of ALC1-KO cells (Figures 7d, 7e, 7f). These data indicate that active, ALC1-catalyzed chromatin remodeling plays a biological role in UV repair.

To validate these observations, we performed immunoblot assays in ALC1-KO cells (Figures 8a-8d). This revealed that the deletion of the chromatin remodeler ALC1 resulted in a delayed repair of 6-4PPs (Figures 8a, 8b) and a strong repair defect of CPD lesions (Figure 8c, d) compared to XPC-KO cells, which were included in parallel. Interestingly, the deletion of ALC1 did not affect the transcription-coupled sub-pathway of NER, as ALC1-KO cells were not sensitive to the drug Illudin S in clonogenic survival assays and did not impact the recovery of RNA synthesis after UV damage, as measured by 5-EU incorporation (Figures S4d-S4e). This suggests that ALC1 specifically acts in GGR. Altogether, these findings demonstrate that both the recruitment of the chromatin remodeler ALC1 to PAR chains and its ability to function as an ATP-driven chromatin remodeler are critical for UV repair.

Discussion

The UV lesion-recognition factor XPC initiates repair of helix-destabilizing DNA lesions, but binds inefficiently to lesions that cause poor helix destabilization. Here, we identify a biochemical complex of XPC with both PARP1 and PARP2 that is key to the PAR-mediated recruitment of the chromatin remodeler ALC1. In turn, ATP-catalyzed chromatin remodeling by the ALC1 helicase powers and promotes efficient CPD repair. Our work identifies a novel XPC-PARP axis that links ALC1-mediated chromatin remodeling to global genome DNA damage repair (Figure 8e).

Proteomic analyses identify PARP1 and PARP2 as intricate interactors of the lesion-recognition protein XPC. This interaction does not only result in the robust PARylation of XPC, but also modulates the PAR response at UV-C lesions. In fact, the deletion of XPC resulted in reduced PAR levels and impaired the efficient recruitment of the PAR-dependent chromatin remodeler ALC1. Our work suggests that XPC acts as a key regulator of PARylation in GGR. Consistent with our findings, several studies identified XPC as a robust target of PARylation *in vitro* and upon exogenous DNA damage treatment of cultures cells with H2O2 (Buch-Larsen et al., 2020; Hendriks et al., 2019; Maltseva et al., 2015). XPC may thus modulate the PAR-response by being a key PARP1/2 target and acceptor of PAR at DNA lesions. In addition, XPC mildly stimulates the PAR-response by enhancing the enzymatic activity of PARP1 and potentially PARP2. Deducing the mechanism of PAR regulation by XPC may help us understand the impact of PARylation on the protein networks involved in GGR.

In several DNA repair pathways, PARP1 is accompanied by a second poly-(ADP-ribose) polymerase, PARP2. The coordinated action of both PARP1 and PARP2 seems to be required for efficient base excision repair and double-strand break repair (Caron et al., 2019; Fouquin et al., 2017; Ronson et al., 2018). However, the precise function of PARP2 has so far largely remained elusive and has not yet been described in nucleotide excision repair. Here, we identify PARP2 as a novel regulator of the GGR response. The protein displays abundant interactions with XPC and especially with the chromatin remodeler ALC1, suggesting that it is tightly linked to the newly identified XPC-PARP axis. Interestingly, while the contribution of PARP2 to the UV-induced PAR response was minor, we found that PARP2 deletion strongly sensitized cells to UV and was important for the repair of difficult-to-repair CPD lesions. This sparks the question whether PARP2 may contribute to GGR independent

of its catalytic activity. Such a mechanism of regulation was proposed previously for the efficient repair of double-strand breaks by homologous recombination, where PARP2 limits 53BP1 accumulation and promotes end-resection independently of its catalytic activity (Fouquin et al., 2017). Alternatively, PARP2 may contribute to the synthesis of distinct PAR chains, such as branched PAR molecules at UV-C lesions. Smaller quantities of branched PAR chains may be necessary to promote efficient GGR by virtue of their recognition by specific DNA repair factors, including potentially ALC1.

The co-factor HPF1 prominently stimulates the PARylation activity of PARP1/2 after H2O2 treatment (Bonfiglio et al., 2017; Gibbs-Seymour et al., 2016), likely through completing the active site of the PARP enzymes by providing a “glutamate finger” for facilitated serine ADP-ribosylation (Blessing and Ladurner, 2020; Sun et al., 2021; Suskiewicz et al., 2020). However, it is not known whether the poly-(ADP-ribose)-response in different repair pathways requires distinct co-factors. Interestingly, while we did not detect an interaction of PARP1 or PARP2 with HPF1 after UV damage, we did observe YBX1 as a new UV-dependent interactor of both PARP1 and PARP2. Moreover, depletion of YBX1 reduced PARylation after UV irradiation. *In vitro* studies have suggested that YBX1 stimulates the PAR activity of PARP1 (Alemasova et al., 2018; Naumenko et al., 2020). It is thus tempting to speculate that YBX1 could act as a biochemical co-factor of PARP1/2 enzymes in GGR. Future work will address the exciting potential impact of YBX1 in the poly-ADP-ribose response in the GGR process.

The newly identified XPC-PARP axis is tightly linked to ALC1-mediated chromatin remodeling in GGR. The deletion of either XPC, PARP1 or PARP2 abrogates, completely abolishes or modulates the timely recruitment of ALC1 to UV-C lesions, respectively. This underlines the tight functional connection between the four proteins. Surprisingly, the recruitment of ALC1 was not effectively impaired by deletion of DDB2, as previously described (Pines et al., 2012). The DDB2-dependent recruitment observed previously was pronounced in the absence of XPA, while being mild in WT cells. Based on our recruitment data, we suggest that the XPC-PARP axis is the dominant route to recruit ALC1 to UV-C lesions. DDB2 may support XPC in recruiting ALC1 in situations of increased or sustained damage, as observed in the absence of XPA. This hypothesis is supported by earlier findings showing that inhibition of PARP enzymes strongly delays GGR-mediated repair also in DDB2-deficient cells (Robu et al., 2017).

Our work identifies a key role of active chromatin remodeling in GGR. ALC1 is an ATP-dependent SNF2-type chromatin remodeler that

is activated by an enzymatic switch upon poly-ADP-ribose binding via its C-terminal macrodomain (Lehmann et al., 2017; Singh et al., 2017). The fast activation of ALC1's chromatin remodeling activity results in the local opening of chromatin around DNA lesions (Sellou et al., 2016). Here, we established that both PAR-binding and active chromatin remodeling by ALC1 are required for efficient GGR. Interestingly, ALC1-KO cells did not reveal any defects in transcription-coupled repair, suggesting that the activity of ALC1 is specifically required for the GGR pathway. In addition, ALC1, together with the poly-ADP-ribose polymerases PARP1 and PARP2, show a strong preference in supporting the repair of CPD lesions, rather than of 6-4PPs. It should be noted that earlier studies also reported delayed 6-4PP repair upon depletion of PARP1 measured by flow cytometry (Robu et al., 2013; Robu et al., 2017).

Given the difficulty in recognition and increased time required for CPD repair, it is likely that this repair pathway requires additional chromatin factors to facilitate the repair of such challenging lesions. While PARP1 and PARP2 could promote chromatin loosening through the establishment of negatively charged PAR chains on chromatin components around the DNA lesion, the chromatin remodeler ALC1 may release the chromatin barrier for efficient repair of CPD lesions through the active sliding of nucleosomes and/or the active remodeling of chromatin-bound DNA repair components, as recently shown for XRCC1 and PARP2 in single-strand break repair (Blessing et al., 2020). This may allow critical steps in GGR, such as the handover of XPC and TFIIH, a process that seems to be tightly controlled by the retention of DDB2 on chromatin (Ribeiro-Silva et al., 2020). We propose that the early recognition of 6-4PPs by XPC and the transient response of the XPC-PARP-ALC1 axis serves as a molecular bookmarking system, which primes chromatin containing difficult-to-repair CPDs for efficient repair at later time-points (Figure 8e). Together, XPC, PARP1/2 and ALC1 appear to do the heavy lifting necessary for efficient CPD repair.

Figure S1

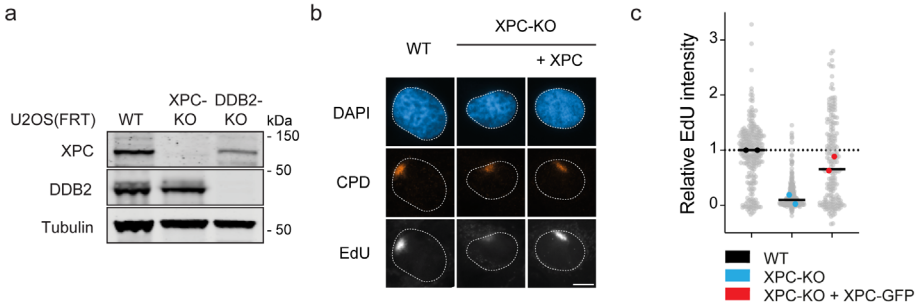

Supplementary Figure 1: Repair defects in XPC-KO cells. (a) Western blot of U2OS (FRT) WT, XPC-KO and DDB2-KO cells. (b) Representative images and (c) quantification of unscheduled DNA synthesis experiments in U2OS (FRT) WT, XPC-KO, XPC-KO + XPC-GFP cells upon UVC irradiation. 191-254 cells were analyzed in two independent experiments. All cells are depicted as individual data points (grey). The median of each biological replicate is depicted as a colored point, while the bar represents the median of all data points.

Figure S2

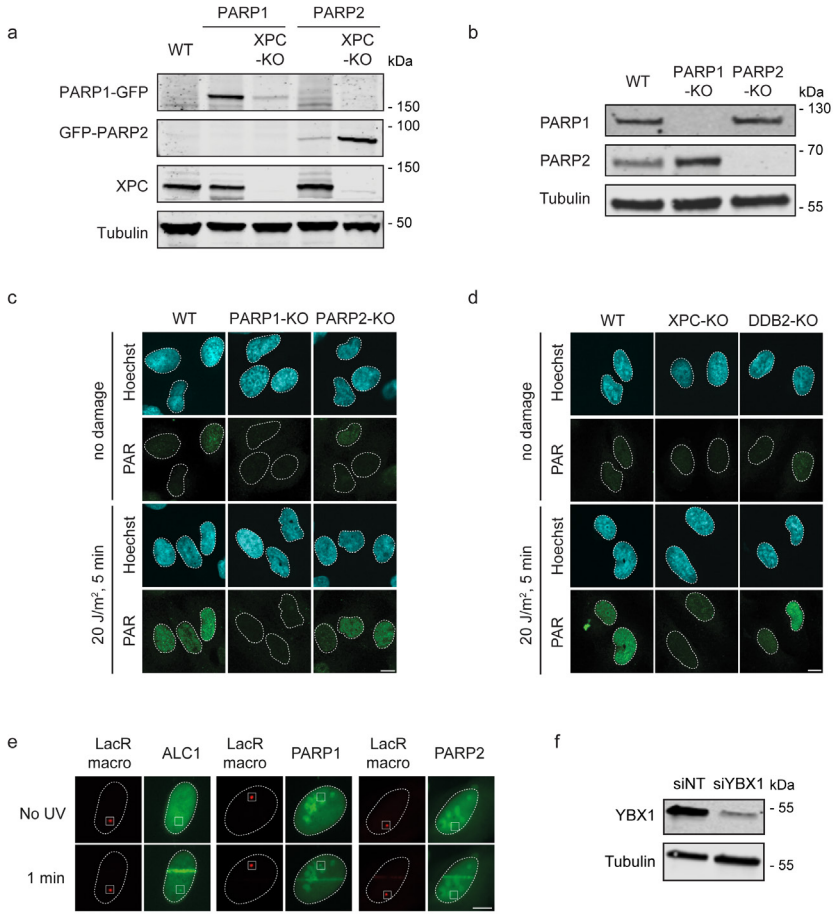

Supplementary Figure 2: Poly-(ADP-ribose) levels at UV lesions. (a) Western blot of U2OS (FRT) WT and XPC-KO cells expressing PARP1-GFP or GFP-PARP2. (b) Western blot of U2OS WT, PARP1-KO and PARP2-KO cells. (c) Representative images of poly-(ADP-ribose) (PAR) levels 5 min after UVC irradiation (20 J/m^2) by immunofluorescence in U2OS WT, PARP1-KO and PARP2-KO cells. (d) Representative images of PAR levels 5 min after UVC irradiation (20 J/m^2) by immunofluorescence in U2OS (FRT) WT, XPC-KO and DDB2-KO cells. (e) Representative images of GFP-tagged ALC1, PARP1 or PARP2 recruitment to the LacO array upon tethering to the indicated mCherry-LacR-macrodomain. Pictures were taken before and 1 min after UV-C micro-irradiation. (f) Western blot of U2OS (FRT) WT cells treated with non-targeting or YBX1 siRNAs for 48h.

Figure S3

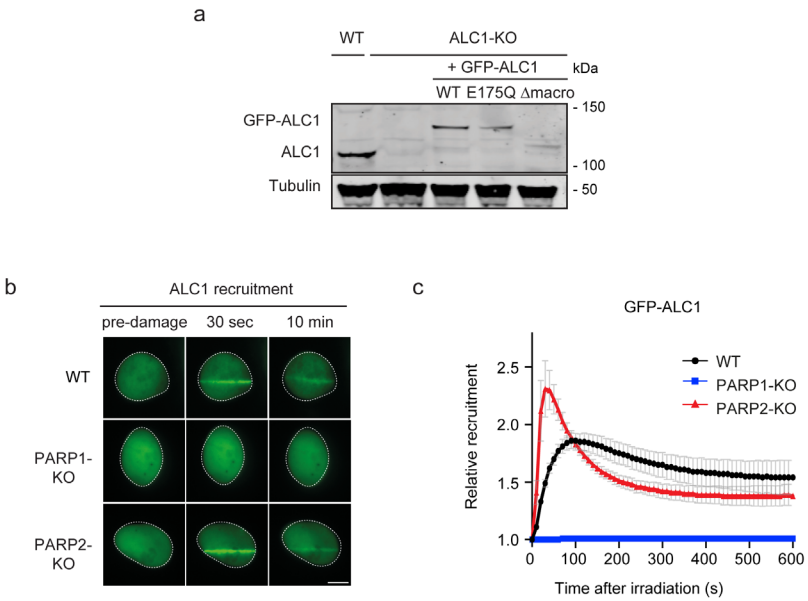

Supplementary Figure 3: 6-4PP repair kinetics in PARP1/2-KO cells. (a) Western blot of U2OS (FRT) ALC1-KO cells expressing GFP-ALC1 WT, GFP-ALC1 E175Q or GFP-ALC1 Δmacrodomain. (b) Differential interactomes of GFP-ALC1 from UVC-irradiated (20 J/m^2, 1 h) vs. unirradiated U2OS (FRT) ALC1-KO cells. (c) Representative images and (d) recruitment kinetics of GFP-ALC1 in U2OS, PARP1-KO and PARP2-KO cells upon UVC irradiation. 53-60 cells were analyzed in two independent experiments. The data are shown as mean + SEM.

Figure S4

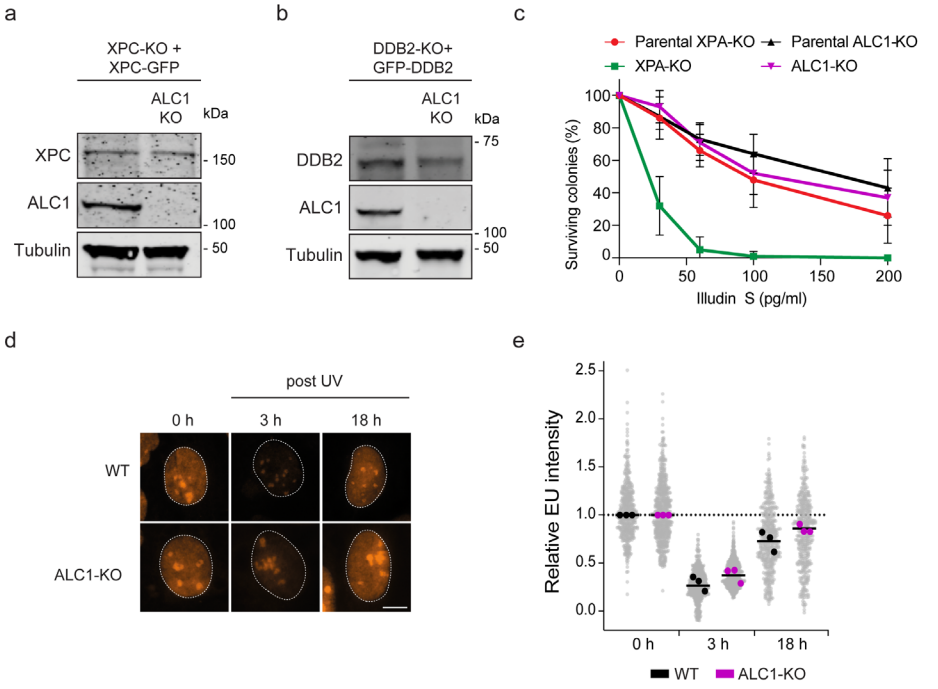

Supplementary Figure 4: Effects of ALC1-KO on NER. (a) Western blot of U2OS (FRT) XPC-KO + XPC-GFP and XPC ALC1-dKO + XPC-GFP cells. (b) Western blot of U2OS (FRT) DDB2-KO + GFP-DDB2 and DDB2 ALC1-dKO + GFP-DDB2 cells. (c) Clonogenic survival assays of U2OS ALC1-KO and U2OS (FRT) CSA-KO cells and the respective parental cell lines upon Illudin S treatment. The data is depicted as mean + SEM from three independent experiments. (d) Representative images and (e) quantification of recovery of RNA synthesis assays after UVC irradiation. 78-212 cells were analyzed in three independent experiments. All cells are depicted as individual data points (grey). The median of each biological replicate is depicted as a colored point, while the bar represents the median of all data points.

Material and methods

Cell lines. All cell lines were cultured at 37°C in an atmosphere of 5% CO_2 in DMEM (Thermo Fisher Scientific/Sigma) supplemented with penicillin/streptomycin (Sigma/GIBCO) and 10% fetal bovine serum (FBS; Bodinco BV/ GIBCO).

Plasmids. The DDB2 gene from the mCherry-NLS-DDB2 plasmid was inserted into the pcDNA5-FRT-TO-Puro-GFP-C1 plasmid as an HpaI/KpnI fragment. The macroH2A1.1-GFP cassette was amplified by PCR and inserted as an EcoRI/BamHI fragment into the mCherry-LacR-NLS-C1. The GFP-ALC1 ∆macrodomain cassette contains an insertion with a stop codon after amino acid 726 and was inserted into pcDNA5/FRT/TO-Hygro plasmid (Invitrogen) as described for pcDNA5/FRT/TO-GFP ALC1 WT and E175Q. The PARP1-GFP (GenBank: BC037545) and GFP-PARP2 cassettes (GenBank: NM_001042618.2) were amplified by PCR and inserted into the pcDNA5/FRT/TO-Hygro (+NheI) plasmid as NotI/XhoI or NheI/NotI fragments, respectively. pcDNA5/FRT/TO-Hygro (+NheI) plasmid was generated by adding a NheI restriction site to the multiple cloning site with primers. The XPC cDNA from XPC-EGFP was digested with NrUI x NotI x NarI and ligated into pcDNA/FRT/TO/Puro digested with NotI x EcoRV.

Generation of knock-out cell lines. To generate knockouts, U2OS(FRT) cells were co-transfected with pLV-U6g-PPB encoding a guide RNA from the LUMC / Sigma-Aldrich sgRNA library targeting a specific gene together with an expression vector encoding Cas9-2A-GFP (pX458; Addgene #48138) using lipofectamine 2000 (Invitrogen). Transfected U2OS(FRT) cells were selected on puromycin (1 µg/ml) for three days, plated at low density after which individual clones were isolated. Knockout clones were verified by western blot analysis.

Generation of doxycycline-inducible cell lines. To generate doxycycline-inducible cell lines, U2OS (FRT) cells were co-transfected with a pcDNA5/FRT/TO vector encoding the respective gene-of-interest, and the pOG44 plasmid, encoding the Flp recombinase, in a 4:1 ratio according to Invitrogen's protocol of the Flp-In Core system. Cells were selected for two weeks with 50 mg/mL hygromycin B (Thermo Fisher Scientific) and expanded. The expression in U2OS (FRT) cell lines was induced with 1 mg/mL doxycycline for 24 h.

Immunoprecipitation for Co-IP. Cells were mock treated or UV-C irradiated (20 J/m^2) and harvested after 1 h. Cell pellets were lysed for 20 min on ice in EBC-150 buffer (50 mM Tris pH 7.5, 150 mM NaCl, 0.5% NP-40, 2 mM MgCl2, protease inhibitor cocktail (Roche)) supplemented with 500 U/mL Benzonase® Nuclease (Novagen). Cell lysates were incubated for 1.5 h at 4°C with GFP-Trap®_A beads (Chromotek). The beads were then washed six times with EBC-150 buffer (50 mM Tris pH 7.5, 150 mM NaCl, 0.5% NP-40, 1 mM EDTA, protease inhibitor cocktail (Roche)) and boiled in Laemmli-SDS sample buffer. For the Co-IP of PARP1/PARP2 with YBX1, a centrifugation step (5 min, 10,000 x g) was included after cell lysis on ice to remove all non-chromatin-binding proteins.

Western blot. Cells were spun down, washed with PBS, and boiled for 10 min in Laemmli buffer (40 mM Tris pH 6.8, 3.35% SDS, 16.5% glycerol, 0.0005% Bromophenol Blue and 0.05 M DTT). Proteins were separated on 4-12% Criterion XT Bis-Tris gels (Bio-Rad, #3450124) in NuPAGE MOPS running buffer (NP0001-02 Thermo Fisher Scientific), and blotted onto PVDF membranes (IPFL00010, EMD Millipore). The membrane was blocked with blocking buffer (Rockland, MB-070-003) for 1 h at RT. The membrane was then probed with antibodies as indicated. An Odyssey CLx system (LI-COR Biosciences) was used for detection.

Mass spectrometry sample preparation. After pulldown, the beads were washed 4 times with EBC-2 buffer without NP-40 and 2 times with 50 mM ammonium bicarbonate followed by overnight digestion using 2.5 µg trypsin at 37°C under constant shaking. Peptides were desalted using a Sep-Pak tC18 cartridge by washing with 0.1% acetic acid. Finally, peptides were eluted with 0.1% formic acid/60% acetonitrile and lyophilized.

Mass spectrometry data acquisition. Mass spectrometry was performed essentially as previously described. Samples were analyzed on a Q-Exactive Orbitrap mass spectrometer (Thermo Scientific, Germany) coupled to an EASY-nanoLC 1000 system (Proxeon, Odense, Denmark). Digested peptides were separated using a 20 cm fused silica capillary (ID: 75 µm, OD: 375 µm, Polymicro Technologies, California, US) in-house packed with 1.9 µm C18-AQ beads (Reprospher-DE, Pur, Dr. Maisch, Ammerburch-Entringen, Germany). Peptides were separated by liquid chromatography using a gradient from 2% to 30% acetonitrile in 0.1% formic acid. For the ALC1 samples and related GFP controls the gradient length was 40 min. For the XPC,PARP1 and PARP2 samples gradient length was 100 min. Every gradient was followed by an increase to 95% acetonitrile and back to 2% acetonitrile in 0.1% formic acid for

chromatography column re-conditioning. Flow rate was set to 200 nl/min for 2 h. The mass spectrometer was operated in positive-ion mode at 2.8 kV with the capillary heated to 250°C. Data-dependent acquisition mode was used to automatically switch between full scan MS and MS/MS scans, employing a top 7 method. Full scan MS spectra were obtained with a resolution of 70.000, a target value of 3x106 and a scan range of 400-2.000 m/z (XPC samples) or 300-1600 m/z (ALC1, PARP1 and PARP2 samples). Higher-Collisional Dissociation (HCD) tandem mass spectra (MS/MS) were recorded with a resolution of 35,000, a target value of 1x105 and a normalized collision energy of 25%. The precursor ion masses selected for MS/MS analysis were subsequently dynamically excluded from MS/MS analysis for 60s and Precursor ions with a charge state of 1 and greater than 6 were excluded from triggering MS/MS events. Maximum injection times for MS and MS/MS were 20 and 120 ms (XPC) or 250 and 120 ms (ALC1, PARP1 and PARP2), respectively.

Mass spectrometry data analysis. All raw data were analyzed using MaxQuant (version 1.6.6.0) as described previously. We performed the search against an in silico digested UniProt reference proteome for Homo sapiens including canonical and isoform sequences (27th May 2019). Database searches were performed according to standard settings with the following modifications. Digestion with Trypsin/P was used, allowing 4 missed cleavages. Oxidation (M), Acetyl (Protein N-term) were allowed as variable modifications with a maximum number of 3. Carbamidomethyl (C) was disabled as a fixed modification. Label-Free Quantification was enabled, not allowing Fast LFQ. iBAQ was calculated. Output from MaxQuant Data was further processed on the Perseus computational platform (v 1.6.7.0) 60. LFQ intensity values were $\log_2$ transformed and potential contaminants and proteins identified by site only or reverse peptide were removed. Samples were grouped in experimental categories and proteins not identified in 4 out of 4 replicates in at least one group were also removed. Missing values were imputed using normally distributed values with a 1.8 downshift ($\log_2$) and a randomized 0.3 width ($\log_2$) considering whole matrix values. Statistical analysis (t-tests) was performed to determine which proteins were significantly enriched in each sample compared with the others. Statistical analysis output tables were further processed in Microsoft Excel for comprehensive browsing of the datasets. Interactive Volcano plots were generated using VolcanoseR 18 and Excel.

Mass spectrometry data availability. The mass spectrometry proteomics data have been deposited to the ProteomeXchange Consortium via the

PRIDE 36 partner repository with the dataset identifier PXD025226. For reviewing purposes, the following credentials can be used: Username: reviewer_pxd025226@ebi.ac.uk, Password: waLw0OpU

UV-C laser micro-irradiation. Cells were grown on 18-mm quartz (UV-C) and placed in a Chamlide CMB magnetic chamber in which growth medium was replaced by CO_2-independent Leibovitz's L15 medium (Thermo Fisher). UV-C laser tracks were made using a diode-pumped solid-state 266 nm Yttrium Aluminum Garnet laser (Average power 5 mW, repetition rate up to 10 kHz, pulse length 1 ns). The laser is integrated in a UGA-42-Caliburn/2L Spot Illumination system (Rapp OptoElectronic). Micro-irradiation was combined with live-cell imaging in an environmental chamber set to 37°C on an all-quartz widefield fluorescence Zeiss Axio Observer 7 microscope, using a 100x (1.2 NA) ultrafluar glycerol-immersion objective (UV-C). The laser system is coupled to the microscope via a triggerbox and a neutral density (ND-1) filter blocks 90% of the laser light. An HXP 120 V metal-halide lamp was used for excitation. Images were acquired in Zeiss ZEN and quantified in Image J.

Unscheduled DNA synthesis (UDS). 180.000 cells were seeded on 18-mm glass coverslips in 12-wells plates in DMEM with 1% FBS. After 24 h, cells were locally irradiated through a 5 µm filter with 30 J/m^2 UV-C. Cells were subsequently pulse-labelled with 20 µM 5-ethynyl deoxyuridine (EdU; VWR) and 1 µM FuDR (Sigma Aldrich) for either 1 h or 4 h. After labelling, cells were medium-chased with 10 µM thymidine in DMEM without supplements for 30 min, and fixed for 15 min with 3.7% formaldehyde in PBS. Cells were permeabilized for 20 min in PBS with 0.5% Triton-X100 and blocked in 3% bovine serum albumin (BSA, Thermo Fisher) in PBS. The incorporated EdU was coupled to Attoazide Alexa Fluor 647 using Click-iT chemistry according to the manufacturer's instructions (Invitrogen). After coupling, the cells were post-fixed with 2% formaldehyde for 10 min and subsequently blocked with 100 mM Glycine. DNA was denatured with 0.5% NaOH for 5 min, followed by blocking with 10% BSA (Thermo Fisher) for 15 min. Next, the cells were incubated with an antibody against CPDs for 2 h, followed by secondary antibodies 1 h, and DAPI for 5 min. Cells were mounted in Polymount (Brunschwig).

RNA recovery assay. 30.000 cells were seeded on 12 mm glass coverslips in 24-wells plates in DMEM with 1% FBS. After 24 h, cells were irradiated with UV-C at a dose of 6 J/m^2 and incubated in conditioned medium for different time periods (0, 3 and 20 h) to allow DNA repair and to restart RNA synthesis. Following incubation, nascent RNA was labelled by

incubating the cells with 400 μM 5-ethynyluridine (5-EU; Jena Bioscience; CLK-N002-10,), which was then visualized with a click-iT mix consisting of 50mM Tris buffer pH8, 60μM Atto Azide (ATTO-TEC; 647N-101), 4mM CuSO4•5H2O, 10mM L-ascorbic acid (Sigma-Aldrich; A0278) and 1:1000 DAPI (ThermoFisher; D1306) for one hour. Cell were washed three times for 5 min with PBS, and mounted on microscope slides (Thermo Scientific) using Aqua Polymount (Polysciences, Inc. #18606).

Clonogenic survival assays. Cells were trypsinized, seeded at low density and mock-treated or exposed to an increasing dose of UV light (2, 4, 6, 8 J/m^2 of UV-C 266 nm) or an increasing dose of Illudin S (Santa cruz; sc-391575) for 72 h (30, 60, 100, 200 pg/mL). On day 10, the cells were washed with 0.9% NaCl and stained with methylene blue. Colonies of more than 20 cells were scored.

C. elegans UV survival assays. C. elegans wild type (Bristol N2), parp-1(ok988) and parp-2(ok344) animals were cultured and assayed. For the germ cell and embryo survival assay, staged young adult animals were irradiated on empty agar plates at the indicated doses using two Philips TL-12 UV-B tubes (40W). Following 24 h recovery on OP50 E. coli culture plates, three adult animals were allowed to lay eggs for 4 h on 6 cm plates seeded with HT115 bacteria, in quintuple for each UVB dose. The number of hatched and unhatched (dead) eggs was counted 24 h later and survival percentage calculated. Results are plotted as average of three independent experiments.

LacO-LacR system for detecting PARylated proteins. U2OS 2-6-3 cells containing 200 copies of a LacO-containing cassette were plated on a 18-mm glass coverslip. The next day the cells were co-transfected with lipofectamine 2000 (Invitrogen) and plasmid DNA for 6 h at 37°C. Next the medium was replaced with DMEM +/+ and incubated overnight at 37°C. Prior to the UV-C micro-irradiation, the medium was replaced with CO_2-independent Leibovitz L-15 medium (Thermo Fisher Scientific) and cells were incubated with 10 μM of PARG inhibitor (Sigma) for 30 min. If indicated the cells were additionally incubated with 10 μM Olaparib. UV-C laser tracks were made using a diode-pumped solid-state 266-nm Yttrium Aluminum Garnet laser (average power 5 mW, repetition rate up to 10 kHz, and pulse length 1 ns). The UV-C laser is integrated in a UGA-42-Caliburn/2L Spot Illumination system (Rapp OptoElectronic). Micro-irradiation was combined with live-cell imaging in an environmental chamber set to 37°C on an all-quartz wide-field fluorescence Zeiss Axio Observer 7microscope, using a 100× (1.2 NA) ultrafluar glycerol-immersion

objective (UV-C). The laser system is coupled to the microscope via a TriggerBox, and a neutral density (ND-1) filter blocks 90% of the laser light. An HXP 120-V metal-halide lamp was used for excitation. Images were acquired in Zeiss ZEN and quantified in ImageJ.

Immunoblot. Immunodot and immunoslot blot assays were performed as previously described 13. DNA was extracted using DNeasy Blood & Tissue Kit (Qiagen 69504). DNA (300ng per well, two to three technical replicates per sample) was vacuum-transferred to a nitrocellulose membrane using the Bio-Dot or BioDot-SF apparatus (Bio-Rad, 1706542/5). Membranes were baked at 80oC in a Bio-Rad's Gel Dryer model 583, blocked in 5% milk in PBS with 0.1% Tween (PBST), washed three times in PBST and incubated with 6-4PP or CPD antibodies overnight at 4oC. Membranes were again washed in PBST and incubated with HRP-conjugated anti-mouse antibodies (ECL Mouse IgG, HRP-linked whole Ab (from sheep), Cytiva, NA931). Damage signal was detected using enhanced chemiluminescence (ECL™ Prime Western Blotting System, GE Healthcare, RPN2232) and exposure in the Bio-Rad ChemiDocTM XRS+ imaging system. Genomic DNA amount loaded onto the membrane was quantified using SYBR™ Gold Nucleic Acid Gel Stain (1:5000 dilution, Invitrogen, S11494), by incubating the membrane with SYBR-Gold solution for 60 min, followed by three washes with PBST. Damage signal was normalized to SYBR-Gold signal using Image Lab version 6.0 from Bio-Rad.

Immunofluorescence microscopy. Immunofluorescence staining was performed as described previously 7. In brief, cells were fixed with 2% paraformaldehyde + 0.1% Triton X-100 for 15 min at room temperature, washed 3x with PBS + 0.1% Triton X-100 and subsequently permeabilized with PBS + 0.1% Triton X-100 for 2x 10 min at room temperature. After blocking the cells in PBS+ (PBS + 0.5% BSA + 0.15% glycine), cells were incubated with the primary antibody, diluted in PBS+, overnight at 4°C. Unspecific antibody staining was removed by washing the cells 5x in PBS + 0.1% Triton X-100. Subsequently, cells were stained with Alexa Fluor 488/568-conjugated fluorescent secondary antibody (Thermo Fisher), diluted 1:500 in PBS+, for 1h at room temperature. Finally, cells were washed 5x with PBS + 0.1% Triton X-100, stained with Hoechst 33342 (Fisher Scientific, 1:5000 in PBS) for 10 min and washed 3x in PBS. The immunofluorescence intensities were measured on a Zeiss AxioObserver Z1 confocal spinning-disk microscope equipped with a sCMOS ORCA Flash 4.0 camera (Hamamatsu), using a Plan-Apochromat 40x/0.95-KOrr air objective or a 40x C-Apochromat/1.2-KOrr water objective.

Nuclear PAR levels. Cells were grown for 24h in 96 well SCREENSTAR plates (Greiner Bio-One) and incubated for 10 min with 1μM of PARG inhibitor (PDD 00017273, Sigma) before irradiation with 20 J/m^2 UV-C light (Stratalinker 1800, Agilent Genomics). After UV-C treatment, the cells were incubated for 5 min at 37°C in the presence of PARG inhibitor, and subsequently fixed and stained for immunofluorescence as described above. Nuclear PAR levels were quantified in ImageJ by thresholding cell nucei using the Hoechst signal and subsequently measuring the mean fluorescent signal of poly-ADP ribose in the nucleus.

XPC immunofluorescence at local UV-C lesions. Cells were grown on coverslips (Fisher Scientific). Before irradiation, the coverslips were covered by 5 μm nanopore filters (Millipore) to allow local UV-C irradiation. The cells were then irradiated with 100 J/m^2 UV-C light (Stratalinker, Agilent Genomics) and fixed 10 min after irradiation. The immunofluorescence was essentially done as described above, with the addition of a denaturation step with 0.07 M NaOH in PBS for 5 min and a second blocking step in PBS+ before incubation with the primary antibody, to allow recognition of CPD lesions. The enrichment of XPC at CPD lesions was quantified in ImageJ. Nuclei and CPD lesions were recognized by thresholding the Hoechst and CPD signal, respectively. The mean fluorescent intensity of XPC and CPD was measured at CPD spots and in the rest of the nucleus. The enrichment of XPC/CPD at UV-C lesions was quantified as followed: mean fluorescence(spot)/mean fluorescence(nucleus background) - 1.

siRNA knockdown. Cells were transfected with 10 nM of siRNA using Lipofectamine RNAiMAX (Invitrogen) according to manufacturer's instructions. A second transfection was performed after 5-6 h recovery time, and cells were incubated for another 48 h before performing experiments.

References

Aboussekhra, A., M. Biggerstaff, M.K. Shivji, J.A. Vilpo, V. Moncollin, V.N. Podust, M. Protic, U. Hubscher, J.M. Egly, and R.D. Wood. 1995. Mammalian DNA nucleotide excision repair reconstituted with purified protein components. Cell. 80:859-868.

Adam, S., J. Dabin, O. Chevallier, O. Leroy, C. Baldeyron, A. Corpet, P. Lomonte, O. Renaud, G. Almouzni and S.E. Polo. 2016. Real-Time Tracking of Parental Histones Reveals Their Contribution to Chromatin Integrity Following DNA Damage. Mol Cell. 64:65-78.

Alemasova, E.E., K.N. Naumenko, T.A. Kurgina, R.O. Anarbaev, and O.I. Lavrik. 2018. The multifunctional protein YB-1 potentiates PARP1 activity and decreases the efficiency of PARP1 inhibitors.Oncotarget. 9:23349-23365.

Ame, J.C., V. Rolli, V. Schreiber, C. Niedergang, F. Apiou, P. Decker, S. Muller, T. Hoger, J. Menissier-de Murcia, and G. de Murcia. 1999. PARP-2, A novel mammalian DNA damage-dependent poly(ADP-ribose) polymerase. J Biol Chem. 274:17860-17868.

Araki, M., C. Masutani, M. Takemura, A. Uchida, K. Sugasawa, J. Kondoh, Y. Ohkuma, and F. Hanaoka. 2001. Centrosome protein centrin 2/caltractin 1 is part of the xeroderma pigmentosum group C complex that initiates global genome nucleotide excision repair. J Biol Chem. 276:18665-18672.

Blessing, C., and A.G. Ladurner. 2020. Tickling PARPs into serine action. Nat Struct Mol Biol. 27:310-312.

Blessing, C., I.K. Mandemaker, C. Gonzalez-Leal, J. Preisser, A. Schomburg, and A.G. Ladurner. 2020. The Oncogenic Helicase ALC1 Regulates PARP Inhibitor Potency by Trapping PARP2 at DNA Breaks. Mol Cell. 80:862-875 e866.

Bonfiglio, J.J., P. Fontana, Q. Zhang, T. Colby, I. Gibbs-Seymour, I. Atanassov, E. Bartlett, R. Zaja, I. Ahel, and I. Matic. 2017. Serine ADP-Ribosylation Depends on HPF1. Mol Cell. 65:932-940.

Buch-Larsen, S.C., I.A. Hendriks, J.M. Lodge, M. Rykaer, B. Furtwangler, E. Shishkova, M.S. Westphall, J.J. Coon, and M.L. Nielsen. 2020. Mapping Physiological ADP-Ribosylation Using Activated Ion Electron Transfer Dissociation. Cell reports. 32:108176.

Caron, M.C., A.K. Sharma, J. O'Sullivan, L.R. Myler, M.T. Ferreira, A. Rodrigue, Y. Coulombe, C. Ethier, J.P. Gagne, M.F. Langelier, J.M. Pascal, I.J. Finkelstein, M.J. Hendzel, G.G. Poirier, and J.Y. Masson. 2019. Poly(ADP-ribose) polymerase-1 antagonizes DNA resection at double-strand breaks. Nat Commun. 10:2954.

Chen, Q., M.A. Kassab, F. Dantzer, and X. Yu. 2018. PARP2 mediates branched poly ADP-ribosylation in response to DNA damage. Nat Commun. 9:3233.

Cheon, N.Y., H.S. Kim, J.E. Yeo, O.D. Scharer, and J.Y. Lee. 2019. Single-molecule visualization reveals the damage search mechanism for the human NER protein XPC-RAD23B. Nucleic Acids Res. 47:8337-8347.

Choi, J.H., S. Gaddameedhi, S.Y. Kim, J. Hu, M.G. Kemp, and A. Sancar. 2014. Highly specific and sensitive method for measuring nucleotide excision repair kinetics of ultraviolet photoproducts in human cells. Nucleic Acids Res. 42:e29.

Ciccia, A., and S.J. Elledge. 2010. The DNA damage response: making it safe to play with knives. Mol Cell. 40:179-204.

El-Khamisy, S.F., M. Masutani, H. Suzuki, and K.W. Caldecott. 2003. A requirement for PARP-1 for the assembly or stability of XRCC1 nuclear foci at sites of oxidative DNA damage. Nucleic Acids Res. 31:5526-5533.

Fouquin, A., J. Guirouilh-Barbat, B. Lopez, J. Hall, M. Amor-Gueret, and V. Pennaneach. 2017. PARP2 controls double-strand break repair pathway choice by limiting 53BP1 accumulation at DNA damage sites and promoting end-resection. Nucleic Acids Res. 45:12325-12339.

Gibbs-Seymour, I., P. Fontana, J.G.M. Rack, and I. Ahel. 2016. HPF1/C4orf27 Is a PARP-1-Interacting Protein that Regulates PARP-1 ADP-Ribosylation Activity. Mol Cell. 62:432-442.

Goedhart, J., and M.S. Luijsterburg. 2020. VolcaNoseR is a web app for creating, exploring, labeling and sharing volcano plots. Sci Rep. 10:20560.

Hendriks, I.A., S.C. Larsen, and M.L. Nielsen. 2019. An Advanced Strategy for Comprehensive Profiling of ADP-ribosylation Sites Using Mass Spectrometry-based Proteomics. Mol Cell Proteomics. 18:1010-1026.

Hoeijmakers, J.H. 2009. DNA damage, aging, and cancer. The New England journal of medicine. 361:1475-1485.

Hoogstraten, D., S. Bergink, J.M. Ng, V.H. Verbiest, M.S. Luijsterburg, B. Geverts, A. Raams, C. Dinant, J.H. Hoeijmakers, W. Vermeulen, and A.B. Houtsmuller. 2008. Versatile DNA damage detection by the global genome nucleotide excision repair protein XPC. J Cell Sci. 121:2850-2859.

Janicki, S.M., T. Tsukamoto, S.E. Salghetti, W.P. Tansey, R. Sachidanandam, K.V. Prasanth, T. Ried, Y. Shav-Tal, E. Bertrand, R.H. Singer, and D.L. Spector. 2004. From silencing to gene expression: real-time analysis in single cells. Cell. 116:683-698.

Lehmann, L.C., G. Hewitt, S. Aibara, A. Leitner, E. Marklund, S.L. Maslen, V. Maturi, Y. Chen, D. van der Spoel, J.M. Skehel, A. Moustakas, S.J. Boulton, and S. Deindl. 2017. Mechanistic Insights into Autoinhibition of the Oncogenic Chromatin Remodeler ALC1. Mol Cell. 68:847-859 e847.

Luijsterburg, M.S., I. de Krijger, W.W. Wiegant, R.G. Shah, G. Smeenk, A.J. de Groot, A. Pines, A.C. Vertegaal, J.J. Jacobs, G.M. Shah, and H. van Attikum. 2016. PARP1 Links CHD2-Mediated Chromatin Expansion and H3.3 Deposition to DNA Repair by Non-homologous End-Joining. Mol Cell. 61:547-562.

Luijsterburg, M.S., J. Goedhart, J. Moser, H. Kool, B. Geverts, A.B. Houtsmuller, L.H. Mullenders, W. Vermeulen, and R. van Driel. 2007. Dynamic in vivo interaction of DDB2 E3 ubiquitin ligase with UV-damaged DNA is independent of damage-recognition protein XPC. J Cell Sci. 120:2706-2716.

Luijsterburg, M.S., M. Lindh, K. Acs, M.G. Vrouwe, A. Pines, H. van Attikum, L.H. Mullenders, and N.P. Dantuma. 2012. DDB2 promotes chromatin decondensation at UV-induced DNA damage. J Cell Biol. 197:267-281.

Maillard, O., S. Solyom, and H. Naegeli. 2007. An aromatic sensor with aversion to damaged strands confers versatility to DNA repair. PLoS Biol. 5:e79.

Maltseva, E.A., N.I. Rechkunova, M.V. Sukhanova, and O.I. Lavrik. 2015. Poly(ADP-ribose) Polymerase 1 Modulates Interaction of the Nucleotide Excision Repair Factor XPC-RAD23B with DNA via Poly(ADP-ribosyl)ation. J Biol Chem. 290:21811-21820.

Masutani, C., K. Sugasawa, J. Yanagisawa, T. Sonoyama, M. Ui, T. Enomoto, K. Takio, K. Tanaka, P.J. van der Spek, D. Bootsma, and et al. 1994. Purification and cloning of a nucleotide excision repair complex involving the xeroderma pigmentosum group C protein and a human homologue of yeast RAD23. EMBO J. 13:1831-1843.

Matsumoto, S., S. Cavadini, R.D. Bunker, R.S. Grand, A. Potenza, J. Rabl, J. Yamamoto, A.D. Schenk, D. Schubeler, S. Iwai, K. Sugasawa, H. Kurumizaka, and N.H. Thoma. 2019. DNA damage detection in nucleosomes involves DNA register shifting. Nature. 571:79-84.

Menissier de Murcia, J., M. Ricoul, L. Tartier, C. Niedergang, A. Huber, F. Dantzer, V. Schreiber, J.C. Ame, A. Dierich, M. LeMeur, L. Sabatier, P. Chambon, and G. de Murcia. 2003. Functional interaction between PARP-1 and PARP-2 in chromosome stability and embryonic development in mouse. EMBO J. 22:2255-2263.

Min, J.H., and N.P. Pavletich. 2007. Recognition of DNA damage by the Rad4 nucleotide excision repair protein. Nature. 449:570-575.

Moser, J., M. Volker, H. Kool, S. Alekseev, H. Vrieling, A. Yasui, A.A. van Zeeland, and L.H. Mullenders. 2005. The UV-damaged DNA binding protein mediates efficient targeting of the nucleotide excision repair complex to UV-induced photo lesions. DNA Repair (Amst). 4:571-582.

Mu, D., C.H. Park, T. Matsunaga, D.S. Hsu, J.T. Reardon, and A. Sancar. 1995. Reconstitution of human DNA repair excision nuclease in a highly defined system. J Biol Chem. 270:2415-2418.

Naumenko, K.N., M.V. Sukhanova, L. Hamon, T.A. Kurgina, E.E. Alemasova, M.M. Kutuzov, D. Pastre, and O.I. Lavrik. 2020. Regulation of Poly(ADP-Ribose) Polymerase 1 Activity by Y-Box-Binding Protein 1. Biomolecules. 10.

Perez-Riverol, Y., A. Csordas, J. Bai, M. Bernal-Llinares, S. Hewapathirana, D.J. Kundu, A. Inuganti, J. Griss, G. Mayer, M. Eisenacher, E. Perez, J. Uszkoreit, J. Pfeuffer, T. Sachsenberg, S.

Yilmaz, S. Tiwary, J. Cox, E. Audain, M. Walzer, A.F. Jarnuczak, T. Ternent, A. Brazma, and J.A. Vizcaino. 2019. The PRIDE database and related tools and resources in 2019: improving support for quantification data. Nucleic Acids Res. 47:D442-D450.

Pines, A., M.G. Vrouwe, J.A. Marteijn, D. Typas, M.S. Luijsterburg, M. Cansoy, P. Hensbergen, A. Deelder, A. de Groot, S. Matsumoto, K. Sugasawa, N. Thoma, W. Vermeulen, H. Vrieling, and L. Mullenders. 2012. PARP1 promotes nucleotide excision repair through DDB2 stabilization and recruitment of ALC1. J Cell Biol. 199:235-249.

Purohit, N.K., M. Robu, R.G. Shah, N.E. Geacintov, and G.M. Shah. 2016. Characterization of the interactions of PARP-1 with UV-damaged DNA in vivo and in vitro. Sci Rep. 6:19020.

Rappsilber, J., M. Mann, and Y. Ishihama. 2007. Protocol for micro-purification, enrichment, pre-fractionation and storage of peptides for proteomics using StageTips. Nature protocols. 2:1896-1906.

Ray Chaudhuri, A., and A. Nussenzweig. 2017. The multifaceted roles of PARP1 in DNA repair and chromatin remodelling. Nat Rev Mol Cell Biol. 18:610-621.

Ribeiro-Silva, C., M. Sabatella, A. Helfricht, J.A. Marteijn, A.F. Theil, W. Vermeulen, and H. Lans. 2020. Ubiquitin and TFIIH-stimulated DDB2 dissociation drives DNA damage handover in nucleotide excision repair. Nat Commun. 11:4868.

Robu, M., R.G. Shah, N. Petitclerc, J. Brind'amour, F. Kandan-Kulangara, and G.M. Shah. 2013. Role of poly(ADP-ribose) polymerase-1 in the removal of UV-induced DNA lesions by nucleotide excision repair. Proc Natl Acad Sci U S A. 110:1658-1663.

Robu, M., R.G. Shah, N.K. Purohit, P. Zhou, H. Naegeli, and G.M. Shah. 2017. Poly(ADP-ribose) polymerase 1 escorts XPC to UV-induced DNA lesions during nucleotide excision repair. Proc Natl Acad Sci USA. 114:E6847-E6856.

Robu, M., R.G. Shah, and G.M. Shah. 2020. Methods to Study Intracellular Movement and Localization of the Nucleotide Excision Repair Proteins at the DNA Lesions in Mammalian Cells. Front Cell Dev Biol. 8:590242.

Ronson, G.E., A.L. Piberger, M.R. Higgs, A.L. Olsen, G.S. Stewart, P.J. McHugh, E. Petermann, and N.D. Lakin. 2018. PARP1 and PARP2 stabilise replication forks at base excision repair intermediates through Fbh1-dependent Rad51 regulation. Nat Commun. 9:746.

Sabatella, M., K.L. Thijssen, C. Davo-Martinez, W. Vermeulen, and H. Lans. 2021. Tissue-Specific DNA Repair Activity of ERCC-1/XPF-1. Cell reports. 34:108608.

Salas-Lloret, D., G. Agabitini, and R. Gonzalez-Prieto. 2019. TULIP2: An Improved Method for the Identification of Ubiquitin E3-Specific Targets. Front Chem. 7:802.

Scharer, O.D. 2013. Nucleotide excision repair in eukaryotes. Cold Spring Harb Perspect Biol. 5:a012609.

Sellou, H., T. Lebeaupin, C. Chapuis, R. Smith, A. Hegele, H.R. Singh, M. Kozlowski, S. Bultmann, A.G. Ladurner, G. Timinszky, and S. Huet. 2016. The poly(ADP-ribose)-dependent chromatin remodeler Alc1 induces local chromatin relaxation upon DNA damage. Mol Biol Cell. 27:3791-3799.

Shah, G.M., F. Kandan-Kulangara, A. Montoni, R.G. Shah, J. Brind'amour, M.D. Vodenicharov, and B. Affar el. 2011. Approaches to detect PARP-1 activation in vivo, in situ, and in vitro. Methods Mol Biol. 780:3-34.

Shieh, W.M., J.C. Ame, M.V. Wilson, Z.Q. Wang, D.W. Koh, M.K. Jacobson, and E.L. Jacobson. 1998. Poly(ADP-ribose) polymerase null mouse cells synthesize ADP-ribose polymers. J Biol Chem. 273:30069-30072.

Singh, H.R., A.P. Nardozza, I.R. Moller, G. Knobloch, H.A.V. Kistemaker, M. Hassler, N. Harrer, C. Blessing, S. Eustermann, C. Kotthoff, S. Huet, F. Mueller-Planitz, D.V. Filippov, G. Timinszky, K.D. Rand, and A.G. Ladurner. 2017. A Poly-ADP-Ribose Trigger Releases the Auto-Inhibition of a Chromatin Remodeling Oncogene. Mol Cell. 68:860-871 e867.

Smith, R., H. Sellou, C. Chapuis, S. Huet, and G. Timinszky. 2018. CHD3 and CHD4 recruitment and chromatin remodeling activity at DNA breaks is promoted by early poly(ADP-ribose)-dependent chromatin relaxation. Nucleic Acids Res. 46:6087-6098.

Sugasawa, K., J.M. Ng, C. Masutani, S. Iwai, P.J. van der Spek, A.P. Eker, F. Hanaoka, D. Bootsma, and J.H. Hoeijmakers. 1998. Xeroderma pigmentosum group C protein complex is the initiator of global genome nucleotide excision repair. Mol Cell. 2:223-232.

Sun, F.H., P. Zhao, N. Zhang, L.L. Kong, C.C.L. Wong, and C.H. Yun. 2021. HPF1 remodels the active site of PARP1 to enable the serine ADP-ribosylation of histones. Nat Commun.

12:1028.
Suskiewicz, M.J., F. Zobel, T.E.H. Ogden, P. Fontana, A. Ariza, J.C. Yang, K. Zhu, L. Bracken, W.J. Hawthorne, D. Ahel, D. Neuhaus, and I. Ahel. 2020. HPF1 completes the PARP active site for DNA damage-induced ADP-ribosylation. Nature. 579:598-602.
Tang, J.Y., B.J. Hwang, J.M. Ford, P.C. Hanawalt, and G. Chu. 2000. Xeroderma pigmentosum p48 gene enhances global genomic repair and suppresses UV-induced mutagenesis. Mol Cell. 5:737-744.
Tapias, A., J. Auriol, D. Forget, J.H. Enzlin, O.D. Scharer, F. Coin, B. Coulombe, and J.M. Egly. 2004. Ordered conformational changes in damaged DNA induced by nucleotide excision repair factors. J Biol Chem. 279:19074-19083.
Tyanova, S., T. Temu, and J. Cox. 2016. The MaxQuant computational platform for mass spectrometry-based shotgun proteomics. Nature protocols. 11:2301-2319.
Tyanova, S., T. Temu, P. Sinitcyn, A. Carlson, M.Y. Hein, T. Geiger, M. Mann, and J. Cox. 2016. The Perseus computational platform for comprehensive analysis of (prote)omics data. Nat Methods. 13:731-740.
van der Weegen, Y., H. Golan-Berman, T.E.T. Mevissen, K. Apelt, R. Gonzalez-Prieto, J. Goedhart, E.E. Heilbrun, A.C.O. Vertegaal, D. van den Heuvel, J.C. Walter, S. Adar, and M.S. Luijsterburg. 2020. The cooperative action of CSB, CSA, and UVSSA target TFIIH to DNA damage-stalled RNA polymerase II. Nat Commun. 11:2104.
Vodenicharov, M.D., M.M. Ghodgaonkar, S.S. Halappanavar, R.G. Shah, and G.M. Shah. 2005. Mechanism of early biphasic activation of poly(ADP-ribose) polymerase-1 in response to ultraviolet B radiation. J Cell Sci. 118:589-599.
Volker, M., M.J. Moné, P. Karmakar, A. van Hoffen, W. Schul, W. Vermeulen, J.H. Hoeijmakers, R. van Driel, A.A. van Zeeland, and L.H. Mullenders. 2001. Sequential assembly of the nucleotide excision repair factors in vivo. Mol Cell. 8:213-224.
Wang, H., L. Zhai, J. Xu, H.Y. Joo, S. Jackson, H. Erdjument-Bromage, P. Tempst, Y. Xiong, and Y. Zhang. 2006. Histone H3 and H4 Ubiquitylation by the CUL4-DDB-ROC1 Ubiquitin Ligase Facilitates Cellular Response to DNA Damage. Mol Cell. 22:383-394